Integrated correction of optical distortions for global HR-EBSD techniques

Clément Ernould, Benoît Beausir, Jean-Jacques Fundenberger, Vincent Taupin, Emmanuel Bouzy

Integrated correction of optical distortions for global HR-EBSD techniques

Clément Ernould [a,b], Benoît Beausir [a,b,*], Jean-Jacques Fundenberger [a,b], Vincent Taupin [a,b], Emmanuel Bouzy [a,b]

[a] Université de Lorraine, CNRS, LEM3, F-57000 Metz, France
[b] Laboratory of Excellence on Design of Alloy Metals for low-mAss Structures (DAMAS), University of Lorraine, 57073 Metz, France

A B S T R A C T

Optical distortions caused by camera lenses affect the accuracy of the elastic strains and lattice rotations measured by high-angular resolution techniques. This article introduces an integrated correction of optical distortions for global HR-EBSD/HR-TKD approaches. The digital image correlation analysis is directly applied to optically distorted patterns, avoiding the pattern pre-processing step conducted so far while preserving the numerical efficiency of the Gauss-Newton algorithm. The correction implementation is first described and its numerical cost is assessed considering a homography-based HR-EBSD approach. The correction principle is validated numerically for various levels of first-order radial distortion over a wide range of disorientation angles (0 to 14°) and elastic strain (0 to 5×10^{-2}). The errors induced when neglecting such distortions as well as the influence of both the radial distortion coefficient and the pattern centre and optical centre locations are quantified. Even when both reference and target patterns are distorted, the correction appears necessary whatever the disorientation between those patterns. The required accuracy on the true distortion parameters for an effective correction is consequently determined.

1. Introduction

The well-established electron backscatter diffraction (EBSD) technique [1] and the emerging off-axis [2] and on-axis [3] transmission Kikuchi diffraction (TKD) techniques are dedicated to the microstructural characterisation of crystalline materials in the scanning electron microscope (SEM). Over the last 25 years, crystallographic orientations have been commonly determined using Hough-transform based indexing (HTI) [4] whose angular resolution is typically 0.5–1° and down to 0.2° [5]. During the last years, the dictionary [6], the spherical harmonic [7,8], and the pattern matching [9–11] approaches have emerged. All using simulated patterns, these orientation determination methods show a higher noise robustness than the HTI, but can also address pseudo symmetries [9]. Using refinement algorithms, they also achieve an angular resolution of up to 0.2° for a well-calibrated system [12,13].

Uncertainties on crystallographic orientations directly affect the accuracy of the disorientation angle and axis [14,15], and so the sensitivity on the geometrically necessary dislocation (GND) density. As highlighted in [16], a standard HTI may miss most of the dislocation structures at disorientations below ~2°. The angular resolution of indexing techniques is thus the limiting factor for the fine characterisation of the deformation structures. To override this limitation, the high-angular resolution EBSD (HR-EBSD) technique was developed in parallel. Since the first attempts by Troost et al. [17] and Wilkinson [18,19], the technique experienced tremendous developments from 2006 under the impetus of Wilkinson et al. [20]. The principle is to capture the displacements visible on the scintillator under the effect of a transformation and to determine the latter knowing the projection geometry and its variations during a beam scan. Using this technique, elastic strains and lattice rotations are determined with an average error on the strain tensor of $\sim1\times10^{-4}$ (0.006°) in a SiGe/Si semiconductor structure or a single crystal of silicon subjected to four-point bending [21].

The displacements are measured using digital image correction (DIC) techniques. The original method [20] is based on local measurements. At least four non-collinear subsets are picked up across two high-resolution electron diffraction patterns, one reference pattern, and one target pattern. In practice, typically 20–100 subsets of 256 × 256 pixels are extracted from patterns of 1000×1000 pixels. Pairs of subsets are then cross-correlated to measure their relative shift with subpixel

accuracy by fitting the near-peak-region of the cross-correlation function with a Gaussian. The technique is, however, insensitive to hydrostatic dilatation of the lattice so the deviatoric elastic deformation gradient tensor $\widehat{\mathbf{F}^e}$ associated with the measured displacement field is obtained by solving iteratively an overdetermined and weighted system of equations [20–22]. The actual elastic deformation gradient $\mathbf{F}^e$ is deduced by assuming a plane-stress condition [23,24]. As proven by Hardin et al. [25], the stress normal to the free surface remains negligible in the absence of stress field sources located near the latter or of a significant error on the specimen tilt angle. In this form, a loss of accuracy is nevertheless observed with increasing disorientation. The shift measurement by cross-correlation is indeed not suitable for images rotated by more than $\sim 7^\circ$ [26]. Maurice et al. [27] and Britton et al. [24] consequently proposed the remapping technique, which consists in warping the reference pattern according to the obtained solution and then repeating the analysis until $\widehat{\mathbf{F}^e}$ converges. In order to avoid iterative remapping, Zhu et al. [28] very recently proposed a one pass remapping based on demons registration.

Benefiting from recent progress in the field of experimental mechanics [29], 'global' HR-EBSD techniques were proposed during the last two years [16,30–32]. They all rely on a single and large subset for which the relative deformations are accounted. Their measurement is performed iteratively in the spatial domain by means of a forward-additive (FA) [30,32] or an inverse-compositional (IC) [16,31] Gauss-Newton (GN) algorithm. It solves the non-linear DIC problem, i.e. the minimisation of the quadratic difference of intensities between the reference subset and the warped target subset. Note that both algorithms have the same convergence rate and accuracy, but the numerical efficiency of the IC-GN algorithm is better [43]. As highlighted by Ruggles et al. [31] and Shi et al. [32], 'global' HR-EBSD approaches are competitive as compared to the 'local' one. An average error of the order of 10^{-5} is notably achieved by Vermeij & Hoefnagels [30] using simulated patterns. In these three works, the relative deformations of the subset are accounted by eight degrees of freedom which are neither more nor less than the components of the deviatoric deformation gradient $\widehat{\mathbf{F}^e}$ ($\widehat{F^e_{33}}$ being 1). These approaches are consequently referred to as integrated-DIC (I-DIC). This is not the case of the fourth approach proposed by Ernould et al. [16], in which a first-order homography is assumed. Such a shape function is often met in photogrammetry to describe projective transformations. It preserves lines, but not angles, i.e. a square is warped into an uncrossed quadrilateral. The GN-algorithm is performed independently of the projection geometry and its variations, which are only required afterwards to analytically deduce $\widehat{\mathbf{F}^e}$ from the measured homography.

Apart from DIC algorithms, numerous factors affect the performances of both the 'local' and the 'global' HR-EBSD techniques. First and foremost, the input signal depends on the thermo-mechanical state of the material (pattern blurring due to plastic strain), the pattern overlapping [33], the camera performances (resolution/binning, sensitivity, and bit depth [34–36]), and the pattern pre-processing (filtering the noise and the continuous background [10] or correcting the optical aberrations [36–38]). Another source of error stems from the uncertainty on the projection geometry, which is ~0.5% of the image width for conventional calibration techniques [39]. Errors of $\sim 3–5\times10^{-3}$ on the elastic strain or lattice rotation components are generated by the latter, but more specifically by the variations of the projection geometry across the orientation map [21,37]. Although the accurate determination of the projection geometry is part of a major research effort [10,37,40–46], the uncertainty inherent to the projection geometry still remains an obstacle to the use of a simulated reference pattern for absolute elastic strain measurements [38,41,47,48], for which the projection geometry should be known with accuracy better than ~0.05% of the image width [21,38,47]. To overcome this issue, Vermeij et al. [49] recently co-correlated strained patterns to resolve absolute elastic strains (i.e. without the need of a strain-free reference). If they demonstrated the potential of such an analysis using (single energy) simulated patterns, experimental validation is required, as stated by the authors.

Due to all these factors, HR-EBSD/HR-TKD techniques are commonly validated using simulated patterns [24,28,30,31,38,49]. More specifically, simulated patterns were used by Britton et al. [38] to assess the error generated by the optical distortions induced by camera lenses. The latter affect the shape of the image and thus interfere with the displacement field associated with the elastic strains and lattice rotations. According to the historical Brown-Conrady model [50–52], optical distortions are mostly divided into radial and tangential contributions, whose effects are illustrated in Fig. 1. Radial distortion stems from the spherical shape of the lens causing disparate light refraction between the centre and the edges. It bends straight lines into circular arcs, depicting either a "barrel" like (Fig. 1b) or a "pincushion" like (Fig. 1c) shape. Those distortions are mostly correlated to the focal length, barrel and pincushion being usually associated with small and long focal length systems, respectively [53]. The tangential distortion (Fig. 1d) stems from the "decentring" [51,52] due to positioning faults, i.e. the misalignment and the non-orthogonality of the optical axes of the lens components, relatively to each other, but also the sensor. In practice, its contribution is often marginal as compared to the radial one [54,55]. Although they are often described mathematically in an independent manner, both radial and tangential distortions are nevertheless physically related [56].

Considering simple barrel distortions of 10^{-8} to 10^{-7}, Britton et al. [38] pointed out that phantom strains of the order of 10^{-3} are induced when an unstrained and undistorted pattern is cross-correlated with its optically distorted version. In this case, careful consideration of optical distortions is essential for any accurate HR-EBSD/HR-TKD measurement [37,38]. However, the authors [38] concluded that such a correction is second order when the reference and target patterns are both subjected to the same optical distortions, especially at low disorientation angles. Optical distortions are also detrimental to the calibration accuracy as recently discussed by Tanaka & Wilkinson [40].

So far, electron diffraction patterns are pre-processed to straighten them before carrying out the DIC analysis. Here, this step is avoided by integrating a correction of the optical distortions directly in the GN-algorithm. The feasibility of such a correction was first mentioned by Vermeij & Hoefnagels [30]. Implemented here in the homography-based approach [16], the proposed correction is easily transferable to I-DIC 'global' HR-EBSD approaches [30–32]. In Section 2, the working principle and the implementation of such a correction are exposed. Its limited computational cost is also assessed in terms of extra execution time. In Section 3, various distortion levels representative of EBSD cameras [37] are considered while the correction is validated from a large set of test patterns with disorientation up to 14° and an equivalent elastic strain ranging from 0 to 5×10^{-2}. In Section 4, the error in elastic strains and rotations induced by the optical aberrations is investigated, first as if the latter were not accounted for and then as if the correction was not exact. More specifically, the level of precision required on the position of the optical axis and the distortion coefficient is evaluated in the case of a first-order radial distortion, whose effect is known to be the most prevalent [53,57].

2. Theoretical and mathematical backgrounds

This section first recalls the constitutive equations of the HR-EBSD technique and briefly introduces the mathematical background of the homography-based DIC approach recently proposed by the authors [16]. Then, the integration of the optical distortion correction into the DIC algorithm is detailed and its numerical extra cost is quantified.

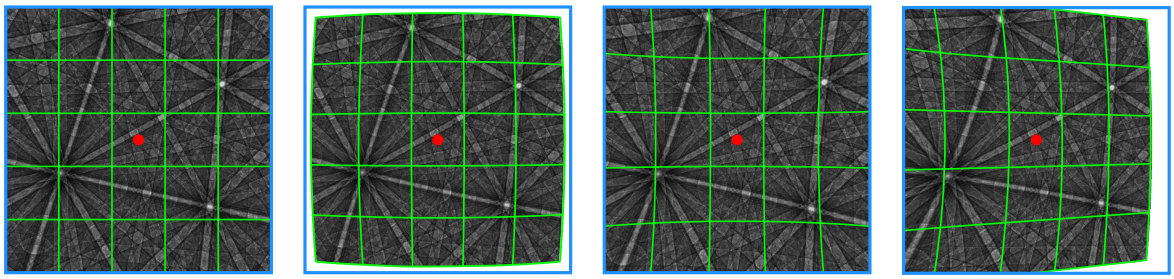

Fig. 1. Simulated electron diffraction pattern subjected to (a) no optical distortion, (b) barrel, (c) pincushion and (d) tangential distortions. The solid green lines highlight the displacements, which are here exaggerated as compared to experimental conditions. The red dot shows the optical centre.

2.1. HR-EBSD problem

In the following, an orthonormal frame $\Re = O(\overrightarrow{X_1}, \overrightarrow{X_2}, \overrightarrow{X_3})$ is attached to the diffraction volume involved in the generation of the reference pattern. As shown in Fig. 2, $\overrightarrow{X_3}$ is perpendicular to the scintillator while $\overrightarrow{X_1}$ and $\overrightarrow{X_2}$ are aligned with the screen width and height, respectively. By definition, the straight $(O, \overrightarrow{X_3})$ intercepts the scintillator at the pattern centre $\mathbf{PC} = [\,0 \quad 0 \quad DD\,]^T$, where DD denotes the sample to detector distance. The displacements visible on the scintillator are related to the elastic deformation gradient $\mathbf{F}^e$ (expressed in $\Re$) through the following equation [20]:

$$\mathbf{X}' = \frac{DD}{(\mathbf{F}^e.\mathbf{X}).\overrightarrow{X_3}}(\mathbf{F}^e.\mathbf{X}), \tag{1}$$

where $\mathbf{X}' = [\,x_1' \quad x_2' \quad DD\,]^T$ is a point in the reference pattern and $\mathbf{X}' = [\,x_1' \quad x_2' \quad DD\,]^T$ its matching point in the target pattern. Note that in this article, the coordinates in the scintillator plane $(\overrightarrow{X_1}, \overrightarrow{X_2})$ are written in lower-case or upper-case letters depending on whether they are expressed relative to the PC or to the upper-left corner of the image (absolute coordinates). The HR-EBSD problem thus consists in registering the diffraction patterns, i.e. identifying the matching points $\boldsymbol{X}$ and $\boldsymbol{X}'$ in order to recover $\mathbf{F}^e$.

The lattice rotations and the elastic strains are then deduced by considering either an infinitesimal framework:

$$\mathbf{F}^e = \mathbf{I} + \boldsymbol{\omega} + \boldsymbol{\varepsilon}$$
$$\text{where } \boldsymbol{\omega} = \begin{pmatrix} 0 & -\omega_3 & \omega_2 \\ \omega_3 & 0 & -\omega_1 \\ -\omega_2 & \omega_1 & 0 \end{pmatrix} \text{ and } \boldsymbol{\varepsilon} = \begin{pmatrix} \varepsilon_{11} & \varepsilon_{12} & \varepsilon_{13} \\ \varepsilon_{12} & \varepsilon_{22} & \varepsilon_{23} \\ \varepsilon_{13} & \varepsilon_{23} & \varepsilon_{33} \end{pmatrix} \tag{2}$$

or a "finite rotation – small strain" theory [27]. The latter implies a left polar decomposition of the deformation gradient tensor into a symmetric stretch matrix $\boldsymbol{v}$, expressing the pure deformation in the configuration rotated by the matrix $\boldsymbol{R}$:

$$\mathbf{F}^e = \mathbf{v}.\mathbf{R} \approx (\mathbf{I} + \boldsymbol{\varepsilon}).\mathbf{R}. \tag{3}$$

This is detailed in Appendix A, in particular regarding the deduction of the lattice rotations ω_i from the R_{ij} components.

As mentioned in the introduction, the technique is insensitive to hydrostatic dilatation of the lattice. The projection of the 3-dimensional diffraction signal on the 2-dimensional scintillator makes the effects of ε_{33} indistinguishable from those of a combination of ε_{11} and ε_{22}. Actually, the deviatoric deformation gradient $\widehat{\mathbf{F}^e} = \mathbf{F}^e / F^e_{33}$ (i.e. ε_{33} is always 0) has to be considered in Eq. (1). Fortunately, the six elastic strain components can be isolated by assuming a traction-free surface condition, which provides an additional relationship based on Hook's law:

$$\in_{33} = -\frac{1}{C_{3333}}[C_{3311}.\in_{11} + C_{3322}.\in_{22} + 2.(C_{3323}.\in_{23} + C_{3331}.\in_{31} + C_{3312}.\in_{12})] \tag{4}$$

where $\in_{ij}$ and C_{ijkl} denote the elastic strain components and the elastic stiffness coefficients expressed in the sample frame.

Finally, it should be recalled than beyond the transformation $\mathbf{F}^e$ itself, the target and the reference pattern also experience a transformation caused by the probe displacement during the beam scan: $\boldsymbol{\delta}\mathbf{PC} = [\,\delta_1 \quad \delta_2 \quad \delta\mathrm{DD}\,]^T$ (Fig. 3). On the one hand, the target pattern is translated by $[\,\delta_1 \quad \delta_2\,]^T$ with respect to the reference one. This quantity corresponds to the displacement of the pattern centre of the target, PC^{TGT}, with respect to the one of the reference, PC^{REF}. On the other hand, the variation δDD of the sample-to-detector distance DD is responsible for an isotropic scaling by a factor $\alpha = (DD - \delta DD)/DD$ with respect to PC^{TGT}. Accounting for these effects is nowadays routinely performed by HR-EBSD methods as shown in the next section.

2.2. Homography-based image registration

The diffraction patterns are registered through a large and unique subset for which the relative deformations are modelled by a first-order homography. Often met in photogrammetry to describe 2D projective transformations, it is also suitable for the HR-EBSD technique as shown in Ernould et al. [16]. Such a parametrisation of the image displacements and displacement gradients implies eight deformation parameters h_{ij}, which are stored in a deformation vector

$$\mathbf{p} = (h_{11}\ h_{12}\ h_{13}\ h_{21}\ h_{22}\ h_{23}\ h_{31}\ h_{32})^T \tag{5}$$

and commonly arranged in a warp (or shape) function $\boldsymbol{W}$ as follows:

$$\mathbf{W}(\mathbf{p}) = \begin{pmatrix} 1+h_{11} & h_{12} & h_{13} \\ h_{21} & 1+h_{22} & h_{23} \\ h_{31} & h_{32} & 1 \end{pmatrix} \tag{6}$$

In this way, the parameters h_{i1}, h_{i2}, h_{i3}, and h_{3i} account for a dilatation, a shear, a translation, and projective effects in the $\overrightarrow{X_i}$ direction ($i = 1,2$), respectively. An illustration of the effect of each deformation parameter is available in [16].

It is necessary to define a centre $\mathbf{X_0} = [\,X_{01} \quad X_{02}\,]^T$ for the homography. The latter arbitrarily coincides with the geometrical centre of the scintillator (see Fig. 2). The point $\boldsymbol{X}$ in the reference pattern and its matching point $\boldsymbol{X}'$ in the target pattern are identified by their position with respect to the homography centre, denoted $\boldsymbol{\xi} = \boldsymbol{X} - \boldsymbol{X}_0$ and $\boldsymbol{\xi}' = \boldsymbol{X}' - \boldsymbol{X}_0$, respectively. They are related to the shape function as follows:

$$\boldsymbol{\xi}' = \boldsymbol{W}(\boldsymbol{p}).\boldsymbol{\xi}. \tag{7}$$

Homogeneous coordinates are considered in this equation. The locations $\boldsymbol{\xi}$ and $\boldsymbol{\xi}'$ are 3-dimensional vectors representing the 2-dimensional

points X and X' of the scintillator plane in Euclidean coordinates, respectively. Unlike Euclidean coordinates, a point admits an infinity of equivalent representations in homogeneous coordinates (see [16] for more details). The first two components of $\boldsymbol{\xi}$ are equal to the Euclidean coordinates if the third one is 1. As a consequence, $\boldsymbol{\xi} = [\xi_1 \quad \xi_2 \quad 1]^T$ is taken as a possible representation of $X - X_0$ since in this case $\xi_i = X_i - X_{0i}$.

The height deformation parameters of the homography are determined iteratively in the spatial domain by means of an inverse-compositional Gauss-Newton (IC-GN) algorithm, similar to all other I-DIC approaches [30–32]. However, the homography-based approach differentiates itself from I-DIC approaches in terms of implementation. I-DIC approaches require the precise knowledge of the projection geometry during the GN algorithm in order to directly obtain the 8 components of $\widehat{\mathbf{F}^e}$ (the ninth being $\widehat{F^e_{33}} = 1$). This also involves integrating the variations of the projection geometry in the GN-algorithm [30,31] or the pre-processing of the diffraction patterns to remove their effects [32]. On the contrary, the homography-based approach does not take into account the projection geometry at all during the GN algorithm. As shown above, the parametrisation of the homography is based on the absolute coordinates of the points forming the subset.

As detailed in Ernould et al. [16], from which the two following equations are extracted, a homography accounts for both the transformation $\widehat{\mathbf{F}^e}$ and the effects due to the variation $\boldsymbol{\delta PC}$ of the projection geometry. The projection geometry and its variations are only considered after the image registration to analytically deduce $\widehat{\mathbf{F}^e}$ from the h_{ij} parameters measured by the IC-GN algorithm. Knowing the position of the homography centre with respect to PC^{REF}, i.e. $\mathbf{X}_0 = [x_{01} \quad x_{02} \quad 0]^T$, those parameters are first corrected into $\widehat{h}_{ij}$ to withdraw the scaling and translation induced by $\boldsymbol{\delta PC}$:

$$\begin{pmatrix} \widehat{h}_{11} & \widehat{h}_{12} & \widehat{h}_{13} \\ \widehat{h}_{21} & \widehat{h}_{22} & \widehat{h}_{23} \\ \widehat{h}_{31} & \widehat{h}_{32} & 1 \end{pmatrix} = \begin{pmatrix} \dfrac{h_{11}+1-\gamma_1.h_{31}}{\alpha} - 1 & \dfrac{h_{12}-\gamma_1.h_{32}}{\alpha} & \dfrac{h_{13}-\gamma_1}{\alpha} \\ \dfrac{h_{21}-\gamma_2.h_{31}}{\alpha} & \dfrac{h_{22}+1-\gamma_2.h_{32}}{\alpha} - 1 & \dfrac{h_{23}-\gamma_2}{\alpha} \\ h_{31} & h_{32} & 1 \end{pmatrix}, \tag{8}$$

where $\gamma_i = \delta_i + x_{0i}.(\alpha - 1)$ with $i = 1, 2$. Note that the expression of γ_i slightly differs from the one previously given by the authors in [16], in which the δ_i were multiplied by α. This stems from the order in which the scale due to a variation in DD and the translation implied by the PC displacement are applied. This is clarified in Appendix B. Finally, the

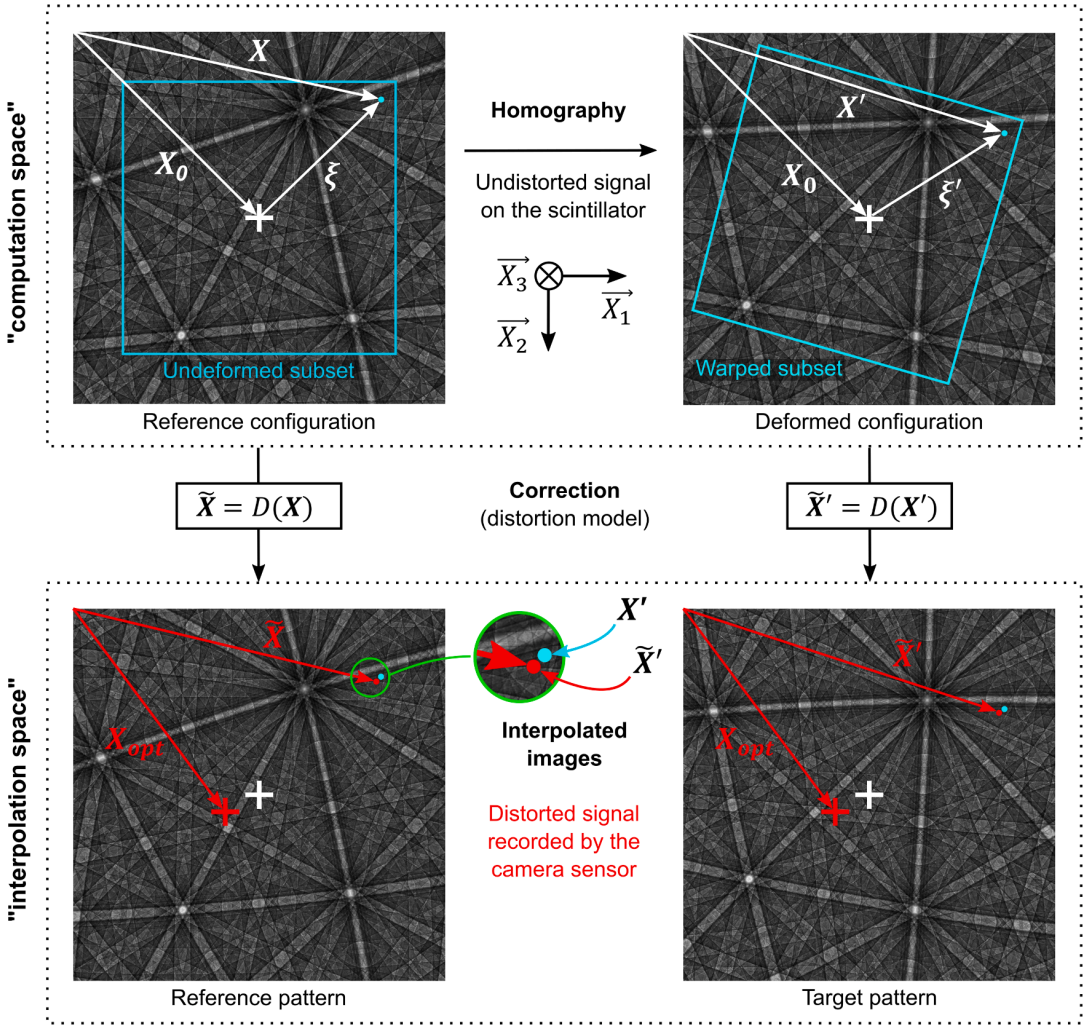

Fig. 2. Principle of the integrated correction. The diffraction patterns are registered in the optically undistorted "computation space" by assuming the first-order homography. Whenever a location is required at location X' (or X) in this space (blue dots), the distortions model D determines the actual location $\tilde{X}'$ (or $\tilde{X}$) to be interpolated in the optically distorted patterns (red dots) forming the "interpolation space".

solution $\widehat{\mathbf{F}^e}$ (expressed in $\Re$) is deduced by a term-by-term identification with Eq. (1), which leads to the following relationships:

$$\widehat{\mathbf{F}^e} = \frac{1}{\beta}\begin{pmatrix} 1+\widehat{h}_{11}+\widehat{h}_{31}.x_{02} & \widehat{h}_{12}+\widehat{h}_{32}.x_{01} & \dfrac{\widehat{h}_{13}-\widehat{h}_{11}.x_{01}-\widehat{h}_{12}.x_{02}+x_{01}.(\beta-1)}{DD} \\ \widehat{h}_{21}+\widehat{h}_{31}.x_{02} & 1+\widehat{h}_{22}+\widehat{h}_{32}.x_{02} & \dfrac{\widehat{h}_{23}-\widehat{h}_{21}.x_{01}-\widehat{h}_{22}.x_{02}+x_{02}.(\beta-1)}{DD} \\ DD.\widehat{h}_{31} & DD.\widehat{h}_{32} & \beta \end{pmatrix} \tag{9}$$

where $\beta = 1-\widehat{h}_{31}.x_{01}-\widehat{h}_{32}.x_{02}$.

2.3. Principle of the integrated correction of the optical distortion

As with all other HR-EBSD methods, the homography-based measurements are only valid provided that the diffraction patterns are optically undistorted. However, camera lenses and mounting defects affect the recorded patterns, for which the displacement field cannot be faithfully modelled by Eq. (1) any more. A possible solution is to preprocess all the diffraction patterns before the analysis. Here, this step is avoided by integrating a correction of optical distortions in the GN-algorithm.

The correction principle is not specific to the homography-based approach, but also transferable to global I-DIC ones. It is based on the distinction between a "calculation space" and an "interpolation space", for which the integrated correction deals as an interface. As Fig. 2 illustrates, the "calculation space" refers to the core of the GN-algorithm, which measures the homography parameters (or the $\widehat{F^e_{ij}}$ components) describing the transformation occurring between two optically undistorted patterns. As its name implies, the "interpolation space" refers to the distorted patterns which are interpolated. Whenever the GN-algorithm requires the signal intensity at position $\boldsymbol{X}$ or $\boldsymbol{X}'$ in the distortion-free reference or deformed configurations, the correction determines their associated locations $\tilde{\boldsymbol{X}}$ or $\tilde{\boldsymbol{X}}'$ to be interpolated into the distorted reference or target patterns, respectively. The correction thus consists of a distortion model D such that $\widetilde{\mathbf{X}} = D(\mathbf{X})$ or $\tilde{\boldsymbol{X}}' = D(\boldsymbol{X}')$.

The nature of D and the position of the optical centre $\boldsymbol{X}_{opt}$ are camera dependant. Consequently, the user has to prescribe them at the beginning of the DIC analysis. The correction principle remains nevertheless unchanged and valid as long as:

(i) All the diffraction patterns amongst a dataset are equally affected by optical distortions, which is reasonably true since they are acquired by the same camera.

(ii) The distortion model D exclusively depends on the input location, which is the case of the most current models [56,58].

2.4. Implementation of the IG-GN algorithm

In the following, the main steps of the IC-GN algorithm are listed for a better understanding of the implementation of both the integrated correction and the homography. For the sake of brevity, the mathematical background and assumptions of the IC-GN algorithm are not exposed. They can be found in the literature [59–61] and more specifically in Ruggles et al.'s paper [31].

During the IC-GN algorithm, the reference subset remains unchanged. It is thus precomputed as well as the Hessian matrix evaluated for $\mathbf{p} = \mathbf{0}$. In ATEX-software [62], the reference subset $\boldsymbol{r}$ is defined as a vector of size N to ease the definition of a subset of any shape. For each location $\boldsymbol{\xi}$ forming the subset, the reference pattern $\boldsymbol{R}$ is interpolated at $\tilde{\boldsymbol{X}}$ (or $\boldsymbol{X}$ in the absence of correction) and the mean value $\bar{r}$ of the so-obtained subset is then subtracted, which gives:

$$\mathbf{r}(\boldsymbol{\xi}) = \mathbf{R}\left(\widetilde{\mathbf{X}}\right) - \bar{r} \quad \text{where} \quad \bar{r} = \sum_{\boldsymbol{\xi}} \mathbf{R}\left(\widetilde{\mathbf{X}}\right). \tag{10}$$

Besides, Δr, the root square of the sum of the squares of $\boldsymbol{r}$ is computed:

$$\Delta r = \sqrt{\sum_{\boldsymbol{\xi}} \mathbf{r}(\boldsymbol{\xi})^2}. \tag{11}$$

Regarding the Hessian matrix, it implies to precompute the steepest descent images, $\mathbf{SDI}(\boldsymbol{\xi}, \mathbf{p})$ ($N\times 8$). To this purpose, $\nabla\boldsymbol{R}(\boldsymbol{\xi})$ ($N\times 2$), the intensity gradients of the reference is multiplied by the Jacobian of the shape function $\mathbf{J_W}(\boldsymbol{\xi}, \mathbf{p})$ (2×8) evaluated for $\mathbf{p} = \mathbf{0}$:

$$\mathbf{SDI}(\boldsymbol{\xi}, \mathbf{p})_{|\mathbf{p}=\mathbf{0}} = \nabla\mathbf{R}(\boldsymbol{\xi})^T.\mathbf{J_W}(\boldsymbol{\xi}, \mathbf{p})_{|\mathbf{p}=\mathbf{0}}. \tag{12}$$

More specifically, this leads to the following calculation:

$$\mathbf{SDI}(\boldsymbol{\xi}, \mathbf{p})_{|\mathbf{p}=\mathbf{0}} = \begin{bmatrix} \vdots & \vdots \\ \nabla R_1\left(\widetilde{\mathbf{X}}\right) & \nabla R_2\left(\widetilde{\mathbf{X}}\right) \\ \vdots & \vdots \end{bmatrix} . \begin{bmatrix} \xi_1 & \xi_2 & 1 & 0 & 0 & 0 & -\xi_1^2 & -\xi_1.\xi_2 \\ 0 & 0 & 0 & \xi_1 & \xi_2 & 1 & -\xi_1.\xi_2 & -\xi_2^2 \end{bmatrix} \tag{13}$$

where $\nabla R_i(\tilde{\boldsymbol{X}})$ denotes the intensity gradient of R along the direction $\overrightarrow{X_i}$ at location $\tilde{\boldsymbol{X}}$ (or $\boldsymbol{X}$ in the absence of correction). Note that $\xi_i = X_i - X_{0i}$,

even in the presence of a correction since the $\boldsymbol{\xi}$ locations are related to the "computation space" (see Fig. 2). Finally, the (symmetric) Gauss-Newton Hessian matrix (8×8) is deduced from the steepest descent images, which will also be reused:

$$\mathbf{H} = \left[\mathbf{SDI}(\boldsymbol{\xi}, \mathbf{p})_{|\mathbf{p}=\mathbf{0}}\right]^T \cdot \left[\mathbf{SDI}(\boldsymbol{\xi}, \mathbf{p})_{|\mathbf{p}=\mathbf{0}}\right]. \tag{14}$$

For each target pattern, the IC-GN algorithm is guided by an initial guess. The algorithm then computes the incremental deformation vector $\boldsymbol{\Delta p}$ and iterates until convergence or until a maximum number of iterations is reached. At each iteration, the following steps are carried out:

1) Compute the warped coordinates $\mathbf{X}' = [X_1' \quad X_2']^T$ using Eq. (7) since $X_i' - X_{0i} = \xi_i'/\xi_3'$ (dividing by ξ_3' is necessary to get back to Euclidean coordinates).
2) If required, correct optical distortions by deducing the location $\tilde{\mathbf{X}}'$ from $\boldsymbol{X}'$ according to the distortion model D.
3) Construct the warped target subsets $\boldsymbol{t}$ by interpolating the distorted target pattern $\boldsymbol{T}$ at location $\tilde{\mathbf{X}}'$ and subsequent computation of Δt, similarly to Eqs. (10) and (11), respectively.
4) Deduce the residuals $\boldsymbol{\delta}$ ($N \times 1$) between the reference and the target subsets:

$$\boldsymbol{\delta}(\boldsymbol{\xi}) = \mathbf{r}(\boldsymbol{\xi}) - \frac{\Delta r}{\Delta t}.\mathbf{t}(\boldsymbol{\xi}). \tag{15}$$

5) Compute the gradient of correlation criterion $\nabla\mathbf{C}$ (8×1):

$$\nabla\mathbf{C}(\mathbf{p}) = \left[\mathbf{SDI}(\boldsymbol{\xi}, \mathbf{p})_{|\mathbf{p}=\mathbf{0}}\right]^T .\boldsymbol{\delta}(\boldsymbol{\xi}). \tag{16}$$

6) Compute of the incremental deformation vector $\boldsymbol{\Delta p}$ by solving the following equation using Cholesky decomposition:

$$\mathbf{H}.\boldsymbol{\Delta p} = -\nabla\mathbf{C}(\mathbf{p}). \tag{17}$$

7) Study the convergence and update the vector $\boldsymbol{p}$ using an inverse-compositional scheme (literal formulas are implemented to avoid the matrix inversion):

$$\mathbf{W}(\mathbf{p}) = \mathbf{W}(\mathbf{p}) \circ \mathbf{W}^{-1}(\boldsymbol{\Delta p}). \tag{18}$$

2.5. Numerical over-cost of the integrated correction

The extra cost of the correction is evaluated by executing the IC-GN algorithm with and without correction and measuring the processing time in both cases. 20,000 iterations are performed ($\boldsymbol{p}$ being reset at the beginning of each one) and the processing time is recorded every 1,000 iterations to ensure that the execution speed is relatively constant. This is the case since the intermediate times do not differ by more than 2% from the average.

The Brown-Conrady distortion model is considered. It accounts for both radial and tangential distortions up to the third order through the distortion coefficients K_i and P_i ($i \in [\![1,3]\!]$), respectively:

$$\begin{pmatrix} \tilde{X}_1 \\ \tilde{X}_2 \end{pmatrix} = \begin{pmatrix} X_1 \\ X_2 \end{pmatrix} + \underbrace{\left(K_1.r^2 + K_2.r^4 + K_3.r^6\right).\begin{pmatrix} \Delta_1 \\ \Delta_2 \end{pmatrix}}_{Radial} + \underbrace{\left(1 + P_3.r^2\right).\begin{pmatrix} P_1.\left(r^2 + 2.\Delta_1^2\right) + 2.P_2.\Delta_1.\Delta_2 \\ P_2.\left(r^2 + 2.\Delta_2^2\right) + 2.P_1.\Delta_1.\Delta_2 \end{pmatrix}}_{Tangential} \tag{19}$$

where $\Delta_i = X_i - X_i^{opt}$ with $i = 1, 2$ and $r = \sqrt{\Delta_1^2 + \Delta_2^2}$

It is chosen since it is widely adopted in the fields of photogrammetry and computer vision [53]. More specifically, Mingard et al. [37] calibrated multiple commercial EBSD cameras using a simplified version of this model.

The correction is accompanied by a lengthening of the calculation time of ~6.2% when using biquintic B-splines for interpolation, for which the 36 B-splines coefficients are precomputed. Note that the result is expressed as a percentage because the processing time is highly dependant on the computer. This percentage is expected to increase if a less computationally demanding interpolation scheme is used, since in the latter case the numerical cost of the IC-GN algorithm decreases while that of the correction remains unchanged. A second measurement is consequently conducted considering bicubic interpolation for which the 16 interpolation coefficients are precomputed as well. The computation lasts ~ 8.2% longer when applying the correction. Such a difference is rather anecdotal given that high order interpolation schemes are recommended for accuracy purpose [29]. Moreover, the intensity gradients can be derived (and interpolated) from the B-splines coefficients, making this type of interpolation particularly consistent with the implementation of the IC-GN algorithm [61].

3. Numerical validation

This section proposes a numerical validation of the homography-based approach and its integrated correction of optical distortions. The generation of the test data is first detailed and the investigated cases are exposed.

3.1. Generation of the test datasets

A dynamically simulated pattern of unstrained aluminium orientated by the triplet of Euler's angles (75°, 125°, 15°) is generated using the open-source software EMsoft 4.2 [63]. The parameters of the simulation are given in Appendix C. A pattern of 2400 × 2400 pixels with a pixel size of 20 μm deals as a "source image", from which smaller patterns of size 1200 × 1200 are extracted, as Fig. 3 illustrates. The latter resolution is chosen accordingly to the Bruker e^-Flash HR+ camera attached to our SEM. For each pixel in the test image, its antecedent in the source image is interpolated. This implies to take into account the transformation $\mathbf{F}^e$, the effects induced by the probe displacement $\boldsymbol{\delta PC}$ as well as the optical distortions.

As indicated by the red disks in Fig. 3, the first step is to determine the location $\boldsymbol{X}'$ in the deformed and optically undistorted configuration associated with each integer-pixel location $\tilde{\mathbf{X}}'$ forming the distorted pattern. In other words, the inverse distortion model D^{-1} such that $\mathbf{X}' = D^{-1}(\tilde{\mathbf{X}}')$ is required. If any distortion model D can be integrated into the DIC analysis, non-linearity issues occur when reversing complex models like the one in Eq. (19). The distortion model is consequently reduced to a first-order radial distortion (i.e. K_1 only) for the purpose of the numerical validation. In this way, exact inverse relationships do exist [53] as detailed in Appendix D. As mentioned in the introduction, the radial distortion has a predominant effect. It is mostly modelled by the first-order term while third and higher-order terms are usually negligible [56].

Once the location $\boldsymbol{X}'$ is identified, the second step is the calculation of its antecedent $\boldsymbol{X}$ by the transformation $\mathbf{F}^e$ in the undistorted and undeformed configuration. If the projection geometry remains constant, this is equivalent to reversing Eq. (1):

$$\mathbf{X} = \frac{DD}{\left(\mathbf{F}^{e^{-1}}.\mathbf{X}'\right).\overrightarrow{X_3}}\left(\mathbf{F}^{e^{-1}}.\mathbf{X}'\right) \tag{20}$$

As mentioned in Section 2.1, the projection geometry varies during a beam scan. To account for those variations, $\boldsymbol{X}'$ should be replaced by

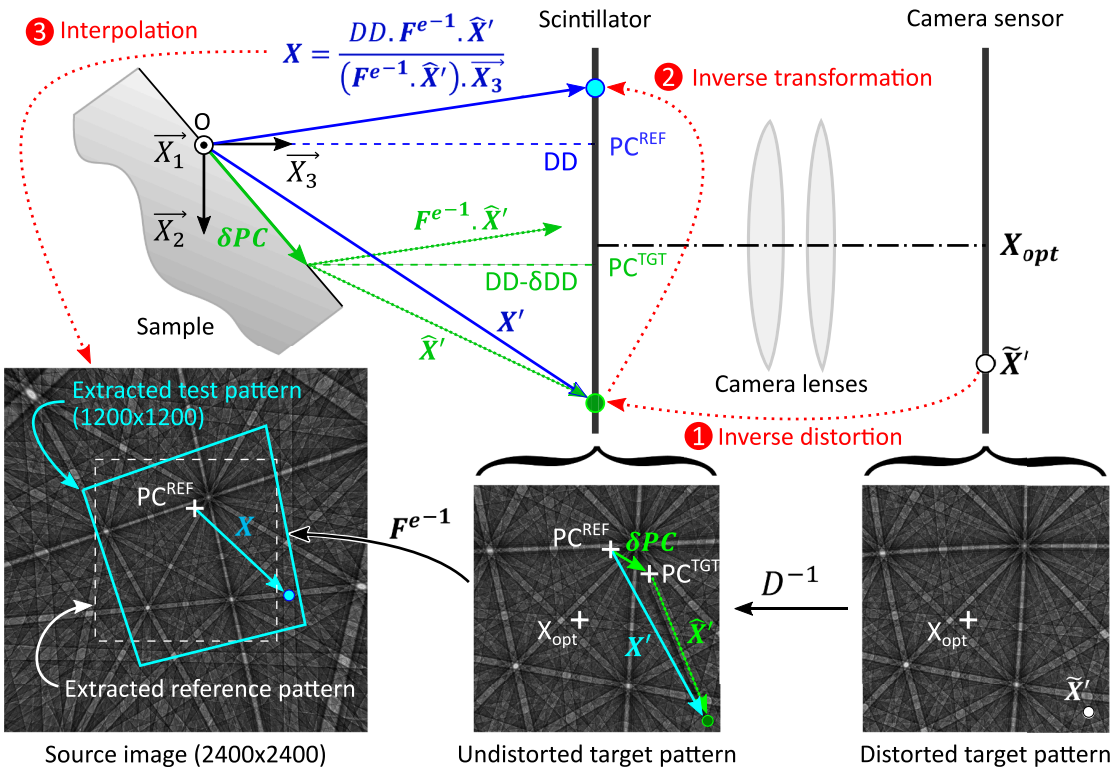

Fig. 3. Sketch of the HR-EBSD geometry. The patterns of size 1200 × 1200 are constructed by interpolating a simulated pattern of unstrained aluminium of size 2400 × 2400 (source image).

$\widehat{X}' = X' - \delta PC$ in Eq. (20) (see Fig. 3). Finally, an offset of 600 pixels is applied to the absolute coordinates of X in order to interpolate the source image, which is twice larger than the generated patterns.

The test patterns are not the result of individual dynamical simulations. Some diffraction effects such as the variation of the band contrast with orientation or a change in the width of the Kikuchi bands in the presence of elastic strains are consequently not reproduced. Although raised by Maurice et al. [27], the influence of the band contrast variations has never been specifically quantified and the authors did not notice an error increase with the disorientation angle (up to 15°) when using dynamically simulated patterns. Recently, Vermeij & Hoefnagels [30] pointed out that the variation in the width of the Kikuchi bands remains a second-order effect, the correlation being according to the authors' words "still very accurate" (i.e. their error remains $<2\times10^{-5}$), even when 1% elastic strain is present. More generally, the principle of the HR-EBSD technique, i.e. Eq. (1), has been largely validated from both simulated [22,24,27,30,31,38] or experimental [20,21,32,64,65] patterns over the past 15 years. Ignoring these diffraction effects is therefore not a hindrance to the validation of the homography-based approach. Indeed, it is sufficient to demonstrate that the displacement field based on Eq. (1) is faithfully measured.

Moreover, the present approach will reveal that the interpolation bias alone can limit the resolution of the HR-EBSD technique to $\sim1\times10^{-4}$. If not specifically mentioned, the interpolation will be performed using the B-splines coefficients. In this way, the test images are generated and registered using the same interpolation scheme (i.e. biquintic B-splines), which strongly reduces the interpolation bias [66]. On the one hand, this allows possible small errors induced by optical distortions to be better observed and quantified. On the other hand, the influence of the interpolation bias on the DIC accuracy can be observed by generating test patterns using a bicubic interpolation of the source image in some cases.

Finally, the avoidance of computationally demanding dynamical pattern simulations enables a large number of cases to be tested, as listed now.

3.2. *Investigated cases and DIC parameters*

The elastic strains ε_{ij} and the lattice rotations ω_i components expressed in the detector frame $\Re$ are given as input, from which the deformation gradient tensor is computed by considering its left polar decomposition in Eq. (3). To allow a direct comparison of the solution measured by the DIC with the input values, ε_{33} will be systematically set to 0.

The method is applied to 1416 test patterns equally divided into two groups:

(i) For the first one (Table 1), the lattice rotations are set such that the disorientation angle $\Delta\theta$ varies from 0.1 to 14°. There are 118 cases: 58 for which the disorientation angle is equally distributed on each one of the three rotation axes and 60 cases for which the disorientation is fully carried on a single axis (20 cases per axis, the values of disorientation angles are in bold in the table). The sign of the rotation is random. For these 118 cases, six elastic strain states are investigated (118 × 6 = 708 patterns in total). As shown in Table 1, these six strain states differentiate themselves from their von Mises equivalent elastic strain ε_{vm}, namely, 0 (unstrained), 5×10^{-4}, 2×10^{-3}, 5×10^{-3}, 1×10^{-2}, and 2×10^{-2}.

(ii) The second group (Table 2) is constructed conversely to the first one. The equivalent elastic strain varies from 1×10^{-4} to 5×10^{-2} so that it encompasses the levels of elastic strains usually observed in metals (i.e. <2 to 5×10^{-3}) as well as the larger one observed in semiconductors (i.e. of the order of 10^{-2}). Similar to the first group, there are 118 cases: 58 for which the elastic strain components are assigned the same absolute value and 60 cases for which all the strain is carried on a single component (12 cases per

Table 1
Overview of the test cases with a disorientation angle ranging from 0.1 to 14°.

118=58+3×20 cases with varying disorientation angle $\Delta\theta$														
58 cases $\omega_{1,2,3} = \pm\Delta\theta/\sqrt{3}$				20 cases* $\omega_1 = \pm\Delta\theta$, $\omega_{2,3} = 0$				20 cases* $\omega_2 = \pm\Delta\theta$, $\omega_{1,3} = 0$				20 cases* $\omega_3 = \pm\Delta\theta$, $\omega_{1,2} = 0$		
where $\Delta\theta \in [0.1°, 14°]$														
*in bold / [°]		**0.10**	0.11	0.12	0.13	0.14	**0.15**	0.16	0.17	0.18	0.19	**0.20**	0.22	0.24
0.26	0.28	**0.30**	0.33	0.37	**0.40**	0.45	**0.50**	0.60	**0.70**	**0.80**	0.90	**1.0**	1.1	1.2
1.3	1.4	1.5	1.6	1.7	1.8	1.9	**2.0**	2.2	2.4	2.6	2.8	**3.0**	3.3	3.7
4.0	4.5	**5.0**	6.0	**7.0**	**8.0**	9.0	**10.0**	10.3	10.7	**11.0**	11.5	**12.0**	**13.0**	**14.0**

6 strain states with varying von Mises equivalent elastic strain ε_{vm}						
ε_{vm}	Unstrained	$\sim 5\times10^{-4}$	$\sim 2\times10^{-3}$	$\sim 5\times10^{-3}$	$\sim 1\times10^{-2}$	$\sim 2\times10^{-2}$
ε_{11} [10^{-4}]	0	1.7	−10	−11	50	83
ε_{12} [10^{-4}]	0	−2.3	6	22	−41	96
ε_{13} [10^{-4}]	0	2.5	−11	24	52	77
ε_{22} [10^{-4}]	0	−1.9	5	16	−44	95
ε_{23} [10^{-4}]	0	2	9	25	−30	83
ε_{33} [10^{-4}]	0	0	0	0	0	0

Table 2
Overview of the test cases with an equivalent elastic strain ranging from 1×10^{-4} to 5×10^{-2}.

118=58+3×20 cases with varying von Mises equivalent elastic strain ε_{vm}														
60 cases $\varepsilon_{ij} = \pm\sqrt{(3.\varepsilon_{vm}{}^2)/16}$ Except for $\varepsilon_{33} = 0$				12 cases* $\varepsilon_{11} = \varepsilon_{vm}$		12 cases* $\varepsilon_{12} = \varepsilon_{vm}$		12 cases* $\varepsilon_{13} = \varepsilon_{vm}$ All other components $\varepsilon_{ij} = 0$		12 cases* $\varepsilon_{22} = \varepsilon_{vm}$		12 cases* $\varepsilon_{23} = \varepsilon_{vm}$		
where $\varepsilon_{vm} \in [1\times10^{-4},\ 5\times10^{-2}]$														
*bold / 10^{-4}		**1**	**2**	3	4	**5**	6	7	**8**	9	**10**	12	14	**16**
18	**20**	22	24	26	28	**30**	32	34	36	38	**40**	42	44	46
48	**50**	52.5	55	57.5	60	62.5	65	67.5	70	72.5	75	77.5	80	82.5
85	87.5	90	95	**100**	125	150	175	**200**	250	300	350	400	450	500

6 disorientation angles $\Delta\theta$						
$\Delta\theta$ [°]	0	~ 0.3	~ 0.6	~ 1	~ 1.5	~ 3
ω_1 [°]	0	0.173	0.346	0.577	0.866	1.732
ω_2 [°]	0	0.173	0.346	0.577	0.866	1.732
ω_3 [°]	0	0.173	0.346	0.577	0.866	1.732

components, ε_{33} is not considered since it is set to 0). These 118 cases are then associated with six disorientation angles, namely 0, 0.3, 0.6, 1, 1.5, and 3°, for which the lattice rotations are equally distributed on each one of the three axes. Small disorientation angles are favoured since accurate elastic strain measurements are usually performed in purely elastically or slightly plastically deformed materials.

A typical projection geometry is considered by placing the pattern centre of the reference pattern at the absolute coordinates $[625 \quad 400]^T$ while *DD* is 16 mm. All the target patterns admit a projection geometry differing by $\boldsymbol{\delta PC} = [5 \quad -3 \quad -1.0919]^T$ pixels, which would be caused by a displacement of the probe of ∼115 μm on a sample surface tilted by 70°. Note that the pixel size being 20 μm, *DD* is here increased by 21.838 μm since the third component of $\boldsymbol{\delta PC}$ (i.e. δDD) is negative. As Fig. 3 illustrates, a positive displacement $\boldsymbol{\delta PC}$ in the $\overrightarrow{X_3}$ direction brings the probe closer to the detector.

The IC-GN algorithm is performed on a square subset of size 901 × 901 pixels located at the centre of the pattern. Biquintic B-splines are systematically considered and the convergence criterion is 0.001 pixel. The initial guess is provided by the cross-correlation based approach introduced in [16], for which a subset of 1024×1024 pixels is used. It relies on successive Fourier-Mellin and Fourier transforms based cross-correlation algorithms, which measure the in-plane rotation and translation between the reference and the target pattern, respectively. The height deformation parameters of the homography are then initialised from these measurements, as detailed in Appendix E. The elastic strain and the lattice rotation components are deduced from the deformation gradient $\widehat{\mathbf{F}^e}$ recovered by the DIC measurements using the "finite rotation – small strain" theory (Eq. (3) and Appendix A).

3.3. Numerical validation of the correction

The error on each elastic strain ε_{ij} or lattice rotation ω_i component is defined as the absolute value of the difference between measures and inputs. In the following, the maximum error *E* amongst all the components will be considered:

$$E = \max\left(\left|\varepsilon_{ij} - \varepsilon_{ij}^{input}\right|, \left|\omega_i - \omega_i^{input}\right|\right) \text{ where } (i,\ j) \in [\![1,3]\!]. \tag{21}$$

First, the test patterns are both generated and registered using biquintic B-spline coefficients and the homography-based approach is applied to optically undistorted patterns (no correction required). This will deal as a comparison basis in terms of accuracy. Since no significant difference in error is observed between the six strain states (Table 1) or the six disorientation angles (Table 2), the error is represented in Fig. 4a, b in the form of a dark-coloured region delimited by the minimum and the maximum of the error E observed amongst those six cases. The maximum errors as a function of the disorientation angle (Fig. 4a) or as a

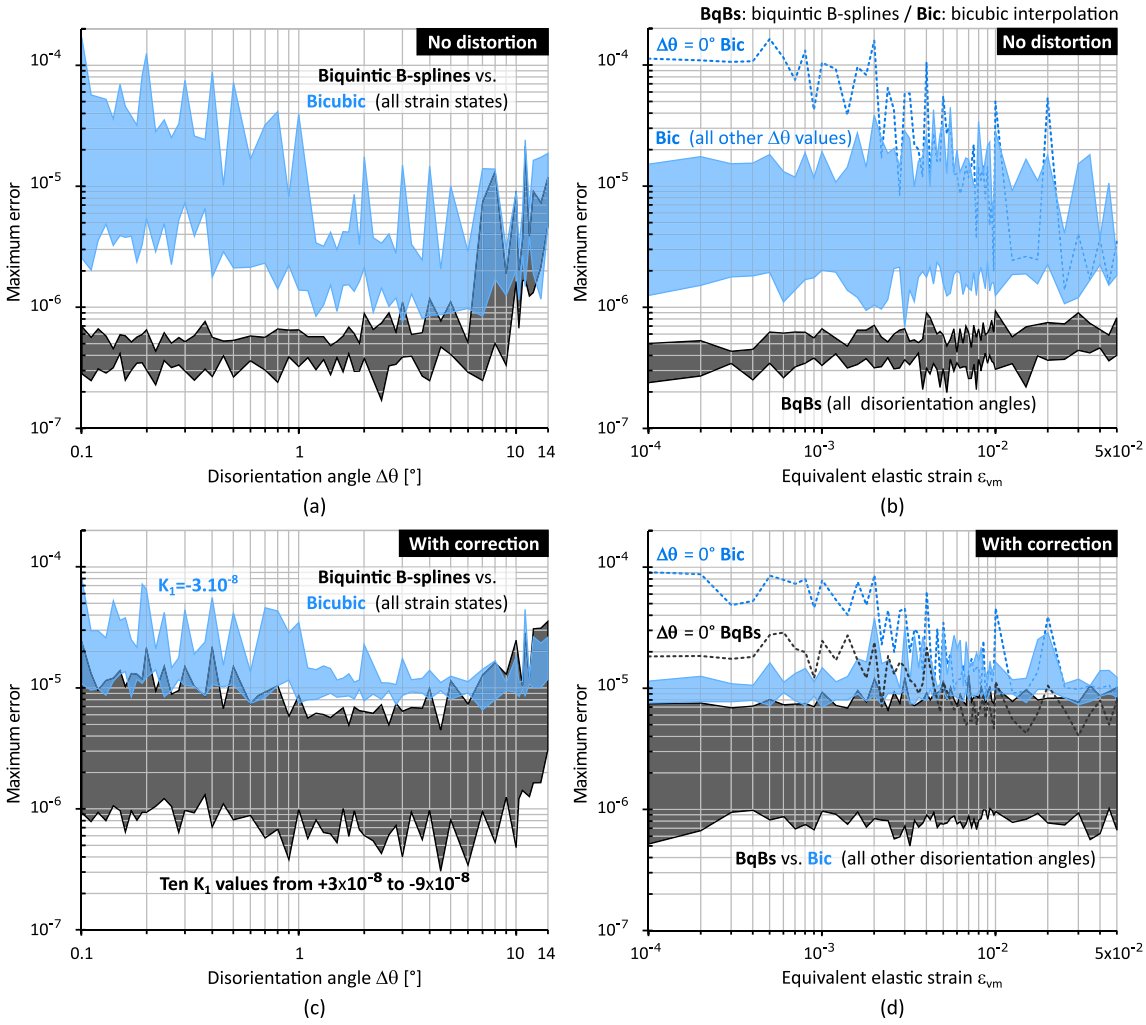

Fig. 4. Error as a function of the disorientation angle (a,c) and as a function of the equivalent elastic strain (b,d) when the DIC analysis is applied without correction to optically undistorted patterns (a,b) or with the correction to optically distorted patterns (c,d). The coloured areas are delimited by the minimum and the maximum of the error amongst all the investigated deformation states (a,c) or disorientation angles (b,d) except regarding $\Delta\theta$=0° (dash lines).

function of the equivalent elastic strain (Fig. 4b) are comparable in terms of both average and maximum values. The mean error is globally of about 5×10^{-7}. In the worst case, a maximum of $\sim 1 \times 10^{-5}$ is observed at the highest disorientation angles for which the warped subset starts to come out of the image, but this remains particularly low anyway.

If such small errors can, of course, be partly attributed to the nature of the test images (noise-free ideal signal), the interpolation bias is also a determining factor. As previously mentioned, the pattern generation adopted in this study enables the interpolation bias to be strongly reduced. To highlight the noticeable influence of the latter on the accuracy, the synthetic experience is repeated, but a bicubic interpolation is used for the pattern generation. The error, reported in blue in Fig. 4a, b, is one order of magnitude higher than previously, but also more scattered. It typically varies from $\sim 1 \times 10^{-6}$ to $\sim 1 \times 10^{-5}$. However, a larger error of $\sim 1 \times 10^{-4}$ is made at the smallest disorientation in Fig. 4a or in the absence of disorientation ($\Delta\theta = 0°$) for equivalent elastic strains ε_{vm} below $\sim 2 \times 10^{-3}$ in Fig. 4b (plotted separately in blue-dash line). For those cases, the interpolation bias may become of the order of the displacements to be tracked, which are amongst the smallest in the dataset. Consistently, the error gradually decreases with the angular disorientation in Fig. 4a while the blue-dash line reaches the level of the other cases as the strain level increases in Fig. 4b. Interestingly, an error of $\sim 1 \times 10^{-4}$ corresponds to the commonly admitted resolution of the HR-EBSD technique.

The homography-based approach is now applied to optically distorted patterns using the proposed integrated correction. Same as previously, the patterns are first generated using biquintic B-splines. Based on Mingard et al. [37], 10 values of K_1 ranging from 3×10^{-8} to -9×10^{-8} are investigated, namely 3, 1, -0.5, -1, -2, -3, -4, -5, -7, -9 ($\times 10^{-8}$). The optical centre $\boldsymbol{X_{opt}}$ is common to all the datasets with a typical shift of $[-30 \quad +20]^T$ pixels with respect to the scintillator centre $\mathbf{X_0}$. The results are summed up in Fig. 4c,d.

For all the investigated K_1 values (dark regions), the error is typical between $\sim 1 \times 10^{-6}$ and $\sim 1 \times 10^{-5}$. It is higher than when using undistorted patterns, especially in the absence of disorientation ($\Delta\theta = 0°$, black dash line in Fig. 4d). Since the formulas are exact from the mathematical point of view [53], such an increase can be attributed to numerical instabilities in the inverse distortion model during the pattern generation. Indeed, very small numbers ($K_1^9 \approx 10^{-63}$) have to be multiplied by very large ones ($r^{18} \approx 10^{52}$). The error nevertheless remains relatively small ($\sim 1 \times 10^{-5}$), which validates the correction principle.

An additional dataset is generated using a bicubic interpolation for $K_1 = -3 \times 10^{-8}$ only, which is typical of the EBSD cameras having a resolution superior to 1000×1000 pixels [37]. Like for the biquintic

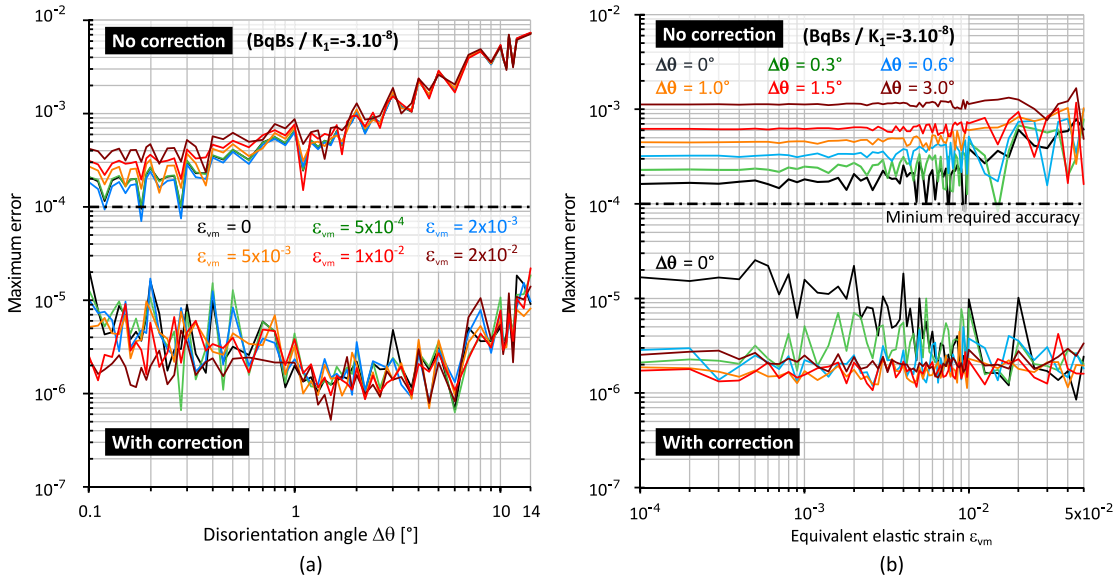

Fig. 5. Error as a function of the disorientation angle (a) and as a function of the equivalent elastic strain (b) when the DIC analysis is applied with or without correction to optically distorted patterns ($K_1 = -3\times10^{-8}$).

B-splines, the minimum error in Fig. 4c,d (bottom of the blue regions) is also higher than in Fig. 4a,b, which is consistent with the alleged numerical instabilities. Note that 'minimum' refers here to the minimum of the maximum error E amongst the six investigated strain states or disorientation angles, not to the actual minimum error on the elastic strain or lattice rotation components. Apart from that, the maximum error and the observed trends remain overall the same.

The present results validate the principle of the integrated correction of the optical distortions for the global HR-EBSD approaches involving a GN-algorithm. Its impact on the accuracy of the DIC analysis is minimal, especially in view of the interpolation bias or the commonly admitted accuracy of $\sim1\times10^{-4}$ of the HR-EBSD/HR-TKD techniques.

4. Influence of the optical distortion on accuracy

Synthetic experiments are relevant for validation purpose, but the distortion model is by definition a limited description of the actual optical distortions. Even if quite complex effects can be faithfully modelled, it must be checked that an approximate correction does not induce greater errors than the aberrations themselves lead to. More precisely, the required accuracy regarding the constants of the distortion model should be evaluated.

The error caused by neglecting the optical aberrations is first assessed for various K_1 values. The influence of the disorientation angle $\Delta\theta$ and the equivalent elastic strain ε_{vm} is discussed as well. The necessity of a correction, even at low disorientation angles, is then demonstrated before investigating the influence of the pattern centre and optical centre locations on the error. Finally, the loss of accuracy due to an approximate correction is evaluated.

4.1. Error in the absence of correction

In this section, the DIC analysis is applied without correction to the distorted datasets from Fig. 4c,d ($K_1 = -3\times10^{-8}$) generated using biquintic B-splines (the bicubic interpolation is no more considered). The results are displayed in Fig. 5a and b, where each one of the solid coloured lines corresponds to a specific strain state or disorientation angle. The errors obtained when using the integrated correction are also reported in the lower part of the figure to ease visual comparison.

In the absence of a correction, the maximum error is always higher than $\sim1\times10^{-4}$. It soars with the disorientation angle (Fig. 5a). This increase is also clearly visible in Fig. 5b for equivalent elastic strains below $\sim5\times10^{-3}$. In comparison, the level of the strain does not affect the error, which remains relatively constant over the investigated range of equivalent elastic strain in Fig. 5b. No clear trend is neither observed in Fig. 5a, especially for disorientations higher than $\sim0.5°$.

The absence of correction is also accompanied by the appearance of oscillations of the error. They highlight that the homography alone cannot fully describe the underlying displacement field. Only a local optimum can be found by the IC-GN algorithm. Noting that the main part of the displacement field is imposed by the lattice rotations, those oscillations are particularly visible in Fig. 5a, for which the chosen magnitude and the sign of the lattice rotation are constantly varying (see the input in Table 1). The oscillation amplitudes also consistently increase with the angular disorientation difference between successive points. As a consequence, the increase of the error with the disorientation angle starts becoming less visible in Fig. 5b as soon as the elastic strains generate displacements as large as the one imposed by the lattice rotations, i.e. for strain levels of about 5×10^{-3} ($\sim0.3°$). However, these oscillations (Fig. 5b for strains $>5\times10^{-3}$) are not such as to call into question the trends observed in Fig. 5a.

Since the equivalent elastic strain shows only a marginal effect on the error, the six curves associated with different strain states in Fig. 5a are averaged and a linear regression is conducted. As shown in Fig. 6, this is repeated to the nine other datasets with varying K_1, each one leading to a coefficient of determination R^2 of about 0.956. Note that no better correlation could be obtained by considering other models such as a second-order polynomial fit, an exponential, or a power law.

The more distorted the patterns, the steeper the increase of the error with the disorientation angle. Actually, both the slope (Fig. 6a) and the y-intercept (Fig. 6b) of the straight-lines fitting the error are proportional to the absolute value of K_1 (with $R^2>0.999$). As discussed later, such a linear dependency is consistent with the literature. The red dash lines in Fig. 6a also highlight that a pincushion distortion (i.e. $K_1 > 0$) induces the same error as a barrel one ($K_1 < 0$) of the same magnitude. Neglecting the radial distortion generates errors higher than 1×10^{-4} even if a relatively small coefficient $K_1 = -5\times10^{-9}$ is present (except below $\sim1°$). More generally, the error is of the order of 1 to 5×10^{-3} for K_1 values between -2×10^{-8} and -4×10^{-8}, which are typical values for EBSD cameras [37]. It can nevertheless be as high as 10^{-2} for stronger

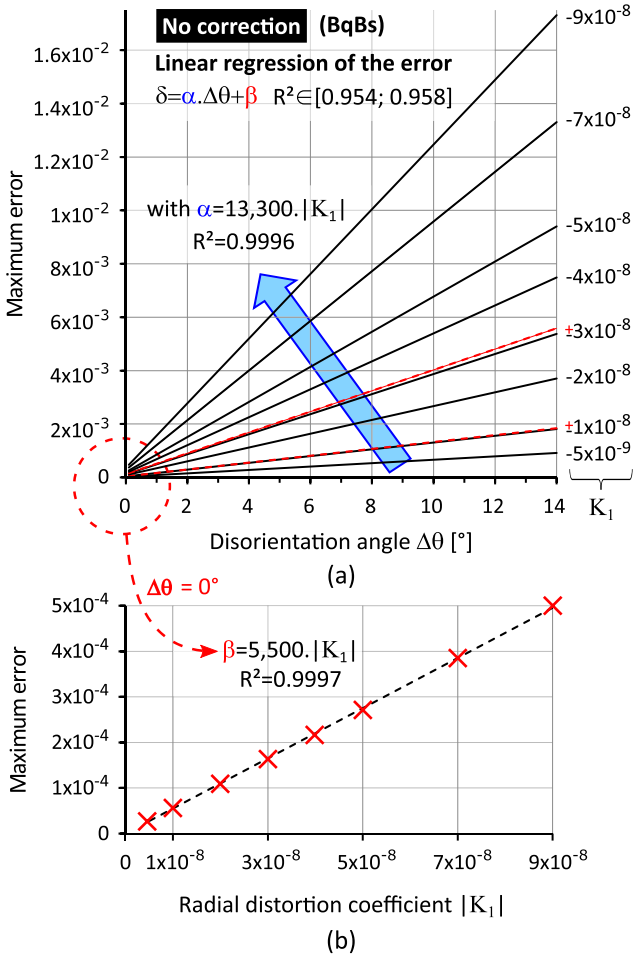

Fig. 6. (a) Linear regression of the error obtained in the absence of correction during the subpixel registration as a function of the disorientation angle. The slope increases linearly with the modulus of the radial distortion coefficient K_1. (b) Linear regression of the error obtained in the absence of disorientation, as a function of the radial distortion coefficient.

radial distortions.

4.2. *On the necessity of a correction*

As shown in Fig. 5a,b, disabling the correction results in an error higher than 1×10^{-4}, even at the lowest disorientation angles, in the case of a typical barrel distortion of $K_1 = -\ 3\times10^{-8}$. Therefore, optical distortion correction is required to ensure that HR-EBSD techniques reach this level of accuracy, even when both the reference and the target patterns are distorted in the same manner.

In addition to the maximum error, the errors on each elastic strain or lattice rotation components are displayed as a function of the disorientation angle in Fig. 7a-c when $\varepsilon_{vm} = 0$, $\varepsilon_{vm}=5\times10^{-3}$ and $\varepsilon_{vm}=2\times10^{-2}$, respectively. These scatter plots are associated with the black, orange, and brown curves of the maximum error in Fig. 5a (no correction). They look quite similar since the influence of the equivalent elastic strain level is marginal as compared to that of the disorientation angle.

Overall, the lattice rotation components ω_1 and ω_2 (dark and light blue dots) present the highest errors, but the applied value is also higher as compared to the elastic strains ($0.1^\circ\approx1.7\times10^{-3}$ radians). The error on ω_3 is smaller, which will be discussed in the next section. Regarding the elastic strain components, the shear ε_{13} (orange dots) is the most affected by the optical distortions. At low disorientation, i.e. $\Delta\theta \leq\sim 0.3^\circ$, the errors on elastic strains may look marginal. However, they need to be compared to the magnitude of the applied values in order to conclude whether optical distortion effects are negligible or not. To this purpose, the relative error on each component or its maximum

$$E_r = \max\left(\left|\frac{\varepsilon_{ij}-\varepsilon_{ij}^{input}}{\varepsilon_{ij}^{input}}\right|,\ \left|\frac{\omega_i-\omega_i^{input}}{\omega_i^{input}}\right|\right) \text{ where } (i,j)\in[\![1,3]\!]. \tag{22}$$

are now considered. Note that when the input value is 0, the relative error of the concerned component is not displayed and omitted in the calculation of the maximum relative error.

Fig. 7d-f show the relative errors on each component as a function of the disorientation angle in cases where $\varepsilon_{vm}=5\times10^{-4}$, $\varepsilon_{vm}=2\times10^{-3}$, and $\varepsilon_{vm}=1\times10^{-2}$, respectively. In addition, Fig. 5a and b (no correction) are replotted in terms of maximum relative error in Fig. 7g and h, respectively. Note that the black curves ($\varepsilon_{vm}=0$ or $\Delta\theta=0^\circ$) are absent since the maximum relative error in those cases would rely on a minority of components, biasing the comparison with the other curves. Perfectly unstrained or lattice rotation free materials are seldom (or never) met in practice anyway.

It arises that the maximum relative error is higher than 10% of the applied value in a quasi-systematic way. The relative errors are all the more significant as the disorientation angle increases (Fig. 7g) or as the level of equivalent elastic strain is low (Fig. 7h). More precisely, relative errors of several tens or hundreds percent are easily made, especially when $\varepsilon_{vm} \leq 2\times10^{-3}$ (Fig. 7h). For those cases, errors of about 1 to 2×10^{-4} induced by a radial distortion of $K_1 = -\ 3\times10^{-8}$ are far from being negligible. As highlighted in Fig. 7d and e, such magnitudes represent 10% to 100% of the applied elastic strain values.

Here, neglecting the optical distortion becomes acceptable (i.e. less than 10% error) only for a large equivalent elastic strain of about 1% or more in the presence of angular disorientations of less than 1°, as shown in Fig. 7f. This scatter plot explains the increase of the relative error observed at low disorientation angles in Fig. 7g, in the presence of large elastic strain ($\varepsilon_{vm} \geq 1\%$, red and brown curves). For those cases, the maximum relative error is prescribed by the relative error on the ω_1 and ω_2 components (light and dark blue dots).

It arises that a typical radial distortion ($K_1 = -\ 3\times10^{-8}$) has to be corrected to accurately measure elastic strains or lattice rotations. Otherwise, an accuracy of about 1 to 2×10^{-4} cannot be reached while making relative errors of several tens or hundreds percent on the elastic strain components. The relative error only appears acceptable (i.e. less than 10%):

(i) Only regarding the elastic strain components when disorientations are below $\sim 1^\circ$, provided that the elastic strain level is of the order of 1% or more.
(ii) Only regarding the lattice rotation components for disorientations higher than $\sim 0.3^\circ$, no matter the elastic strain level.

In order to determine the extent to which the present results are generalisable, the influence of the *PC* and optical centre locations on the error is now investigated.

4.3. *Influence of the pattern centre and the optical centre locations*

Six datasets only differing by the position of their pattern centre and their optical centre are generated. They are designated by the letters from A to F in Fig. 8, in which the absolute coordinates of the pattern centre and the optical centre are given and illustrated. The PC locations are chosen such that typical EBSD (A, B, C), off-axis TKD (D), and on-axis TKD (E, F) configurations are considered. The optical centre is either off-centre as before (A, D, E), or it coincides with the pattern centre (C, F) or it is at the centre of the image without coinciding with the pattern centre (B). These datasets are all subjected to a typical distortion of $K_1 = -3\times10^{-8}$ and the projection geometry is not

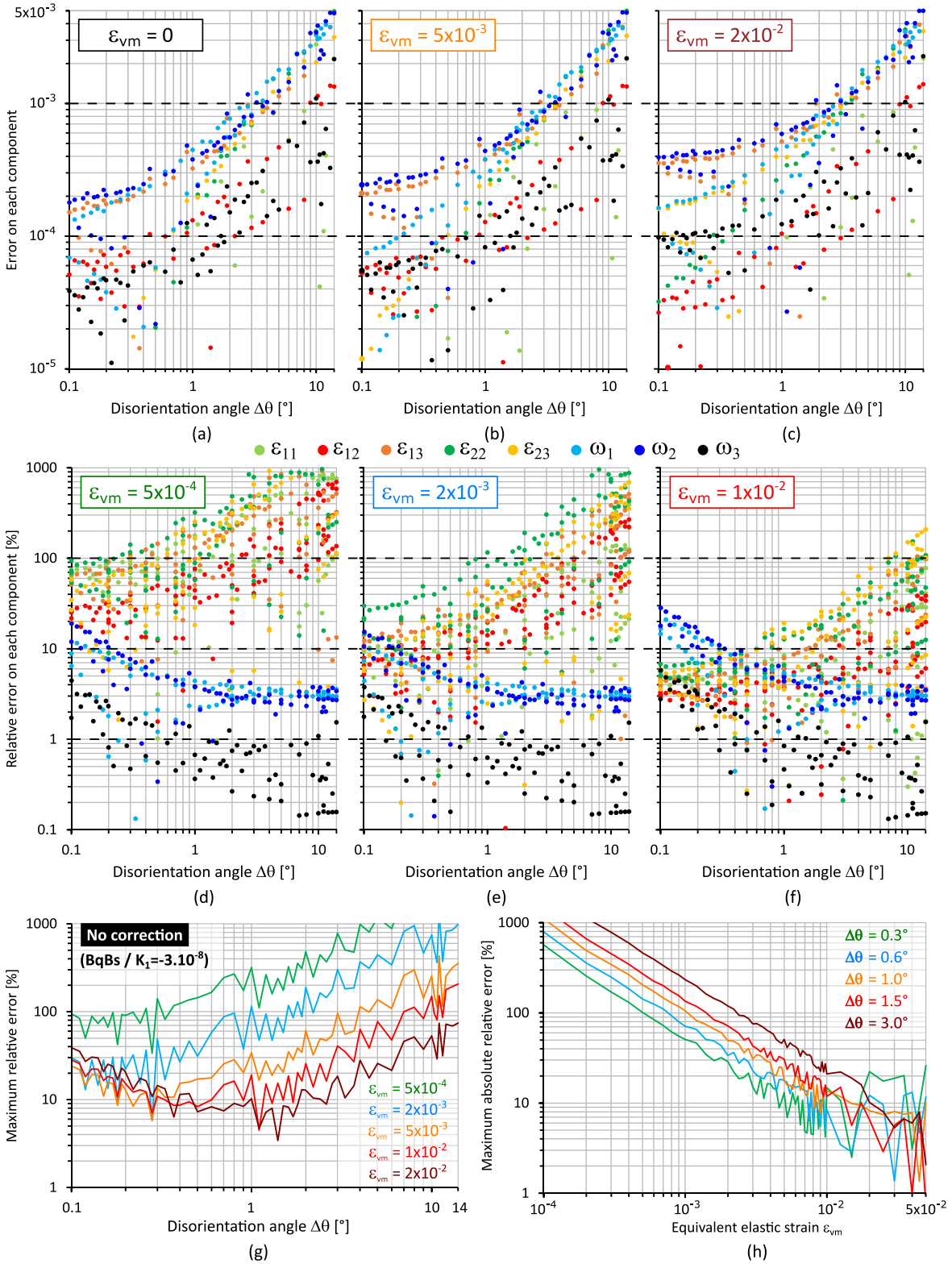

Fig. 7. (a-c) Errors and (e-f) relative errors on each elastic strain or lattice rotation components when a radial distortion of coefficient $K_1 = -3 \times 10^{-8}$ is neglected, in the cases where ε_{vm} is equal to (a) 0, (b) 5×10^{-3}, (c) 2×10^{-2}, (d) 5×10^{-4}, (e) 2×10^{-3}, and (f) 1×10^{-2}. (g-h) Maximum relative error as a function of (g) the disorientation angle $\Delta\theta$ and (h) the equivalent elastic strain ε_{vm} (same dataset as in Fig. 5).

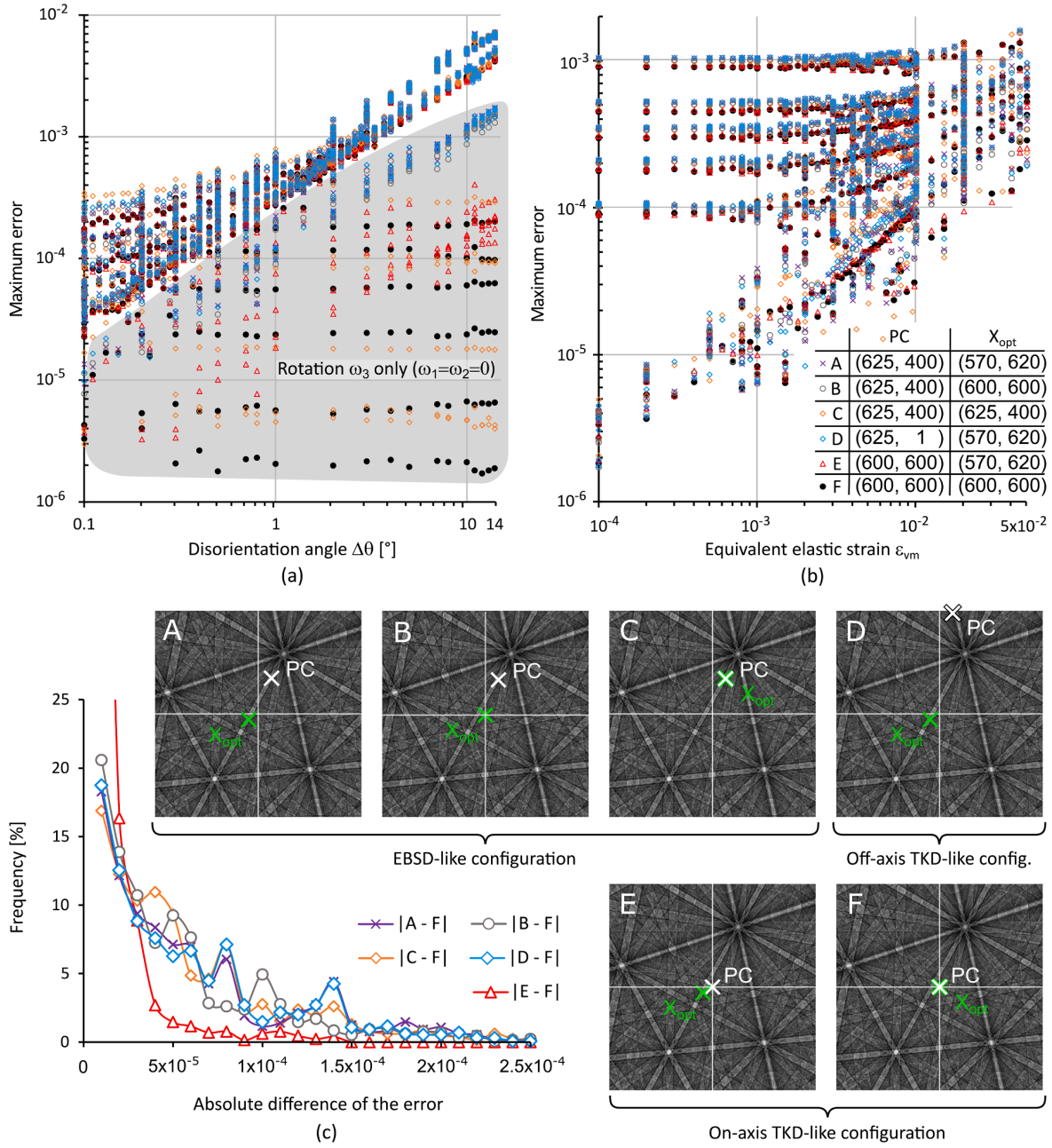

Fig. 8. Influence of the pattern centre and the optical centre positions on the error. (a) Error as a function of the disorientation angle. (b) Error as a function of the equivalent elastic strain. The table gives the absolute coordinates of the pattern and optical centres for the investigated cases A to F illustrated on the diffraction patterns. (c) Distribution of the differences (in absolute value) of the maximum error of each dataset with respect to *F*.

varying ($\boldsymbol{\delta PC} = \mathbf{0}$).

The DIC analysis is conducted without correcting the optical distortions. The maximum error of each one of the 1416 investigated cases is displayed on the scatter graph in Fig. 8a-b. No significant difference is visible between the six datasets, except for some points in the bottom region of Fig. 8a. The latter actually corresponds to the special cases where the rotation is purely in-plane ($\omega_1 = \omega_2 = 0$). The rotation ω_3 is measured correctly when the PC and the optical centre coincide, i.e. for the datasets C (orange diamonds) and F (black dots), for which the errors are only related to the presence of elastic strains.

To better quantify the differences between the datasets, the error of "F" (centred and coinciding optical and pattern centres) is taken as a reference. All the points from Fig. 8a-b are considered except the not suitable special cases mentioned above. The distributions of the error differences in Fig. 8c show that the absolute differences are almost always below 1.5×10^{-4} which is marginal as compared to the errors induced by the negligence of the distortion itself. From this standpoint, the positions of the pattern centre and optical centre are not determinant for the error induced when neglecting the optical aberrations (of typical radial distortion coefficient $K_1 = -3\times10^{-8}$). Therefore, the different SEM-configurations are expected to be affected similarly by the presence of optical distortions.

4.4. *Required accuracy on the correction parameters*

Based on the previous results, only the case A is now considered (off-

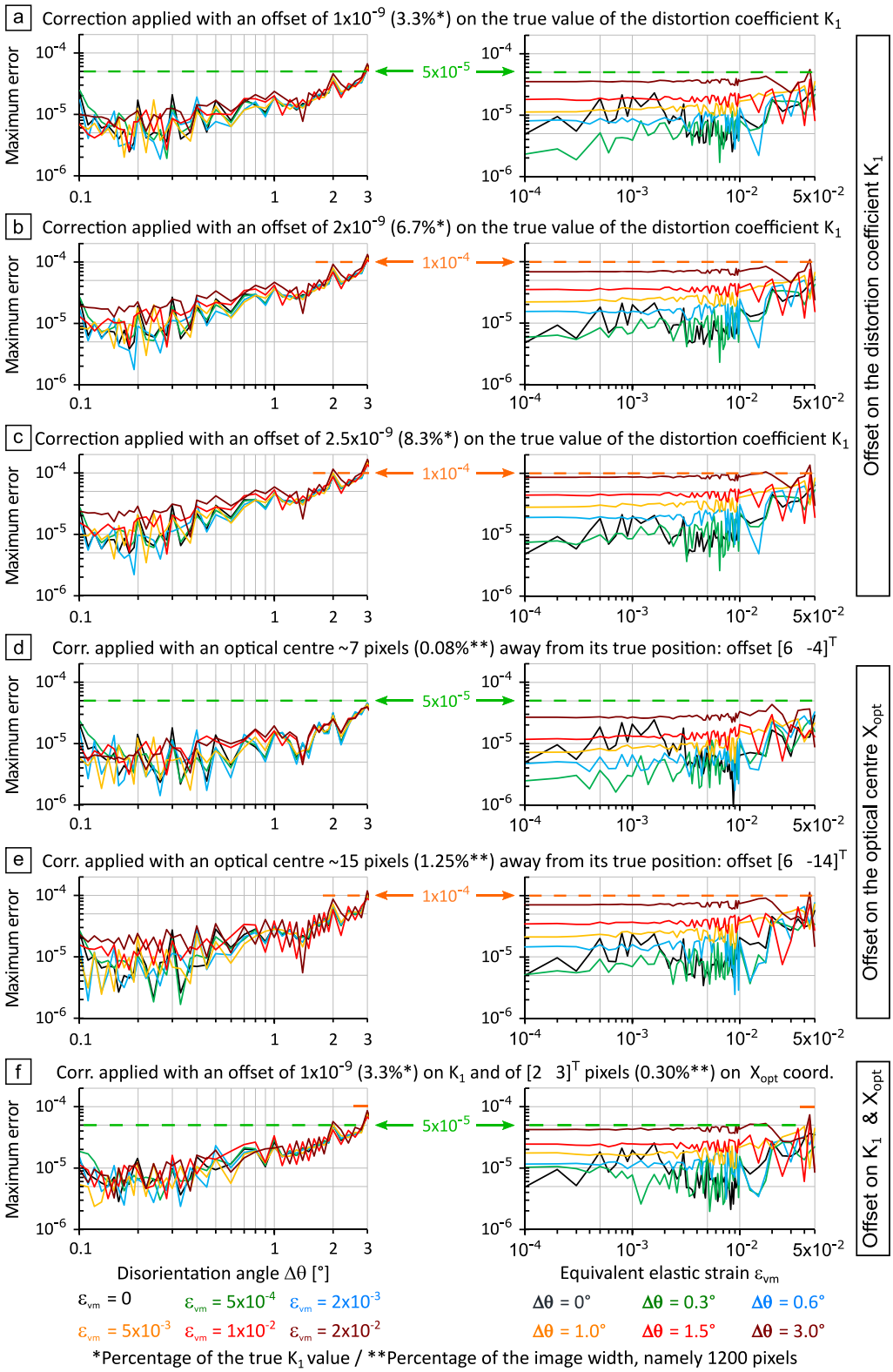

Fig. 9. Error associated with the use of erroneous correction parameters.

centred and non-coinciding optical and pattern centres). The DIC analysis is performed using erroneous correction parameters. The maximum offsets such that the error remains below 1×10^{-4} for disorientation angles smaller than 3° is investigated. Larger disorientation angles are discarded because they are mostly associated with plastically deformed materials for which pattern blurring prevents both SEM calibration [40] and elastic strains [32,16] to be accurately determined.

First, an offset is applied either to the optical centre absolute coordinates, $[570 \quad 620]^T$ pixels, or to the radial distortion coefficient $K_1 = -3\times10^{-8}$. Numerous calculations were performed. They first revealed that applying an offset on the true coefficient K_1 or neglecting a distortion of the same magnitude induce a similar error. As might be expected from Fig. 6a, in which pincushion and barrel distortions were shown to imply the same error, it is equivalent to underestimate or overestimate K_1.

Relevant calculations regarding the required accuracy on the correction parameters are displayed in Fig. 9. An offset of magnitude $\pm1\times10^{-9}$ on K_1 is acceptable as the error remains below 5×10^{-5} (Fig. 9a). Note that the error reaches 1×10^{-4} for disorientation angles of ~6.5°. However, such an error is already made for ~3° when the offset is between 2×10^{-9} (Fig. 9b) and 2.5×10^{-9} (Fig. 9c). Regarding the optical centre, the error remains below 5×10^{-5} for all the investigated cases as long as the prescribed position is not farther than ~7 pixels of the true position (Fig. 9d). The error reaches 1×10^{-4} for disorientations of about 3° when the prescribed optical centre is ~15 pixels away from its true position (Fig. 9e).

Finally, computations are made with an optical centre shifted from its true position by 1 to 3 pixels as well as a K_1 coefficient experiencing an error of 1×10^{-9}. The error remains mostly below 5×10^{-5} and systematically below 1×10^{-4} for all the investigated cases (Fig. 9f).

5. Discussion

The synthetic experiments carried out in this work show that more accurate elastic strain measurements can be performed on optically distorted patterns directly by integrating a distortion model in the GN-algorithm. The accuracy of the 'global' HR-EBSD approach conducted here is not affected by the integrated correction. As addressed in Section 3.3, the observed differences in the error levels, in the absence (Fig. 4a and b) or the presence of a correction (Fig. 4c and d), are 'only' visible because (i) special attention was paid in the reduction of the interpolation bias (ii) numerical instabilities occur with the inverse distortion model, which is not required in practice. It is clear that the correction will not introduce noticeable error in experimental applications unless an inappropriate distortion model or erroneous distortion coefficients are prescribed by the user. The correction principle remains just the same for TKD patterns, on which global DIC has already been applied when using the "on-axis" configuration [16,67].

The test patterns considered in this study were not dynamically simulated patterns. A typical error of $\sim5\times10^{-7}$ is consequently achieved in optical distortion-free patterns. This error is expected to be higher when some diffraction effects such as the variation of the band contrast with changing orientation or variations in the width of the Kikuchi bands under the presence of elastic strains are correctly accounted for in the input images. Based on the literature, the impact of those effects on the accuracy of the HR-EBSD technique seems however marginal, as detailed in Section 3.1. Only the results obtained in the presence of very large elastic strains about 2 to 5% might be subject to discussion, although the work by Vermeij & Hoefnagels [30] tends to indicate that the mechanical model of the HR-EBSD technique, Eq. (1), is still acceptable. Anyway, the spirit of this study is rather to investigate the effects of optical distortions rather than the homography-based DIC approach [16,67] itself. Therefore, the results in Section 3.3 serve mainly to show that the errors observed in this study are almost exclusively due to optical distortions.

Moreover, the image generation adopted in the present work also highlighted that the influence of the interpolation scheme on the accuracy is at least as important as the not reproduced diffraction phenomena (which can also be subjected to simulation errors). As observed in Fig. 4 and 5, the error is typically $\sim5\times10^{-6}$ ($\sim3\times10^{-5}$ in the worst case) for optically distorted patterns when the test images are generated using the biquintic B-splines coefficients whereas the use of a bicubic interpolation scheme leads to errors of $\sim1\times10^{-4}$ at the smallest disorientation angles. Yet, the DIC analysis is executed using exactly the same code and parameters. Note that using bicubic interpolation, Britton et al. [24] achieved accuracy of about 2×10^{-4} on dynamically simulated patterns as they proposed the remapping technique.

First raised by Maurice et al. [42], the influence of the interpolation bias on accuracy has become an increasingly inevitable topic, first with the introduction of the remapping technique and nowadays with the emergence of global DIC approaches for the subpixel registration [16, 30–32] or new algorithms for one pass remapping [28]. Ruggles et al. [31] indicated that they preferred cubic B-splines to more computationally demanding biquintic B-splines since the accuracy improvement was marginal. Although no quantitative indication is given, such observation underlines the necessity to determine the optimal interpolation scheme for HR-EBSD, in particular regarding the elastic strain measurements performed in the presence of low lattice rotations (i.e. $<$ ~0.5°).

By avoiding the uncertainties inherent to the simulation software while minimising the influence of the interpolation bias, the pattern generation routine adopted in this study eased the investigation of the error due to the presence of optical aberrations over a large number of cases (1416 per dataset). More precisely, the DIC analysis and its integrated correction were validated from various strain levels up to 5×10^{-2} in the presence of angular disorientations up to 14°. Values were notably prescribed on the ε_{13} and ε_{23} out of plane shear components while numerical validations from the literature mostly apply normal deformations.

As shown in Section 4, when neglected, a first-order radial distortion induces an error on the elastic strain or lattice rotation components which increases linearly with the absolute value of the distortion coefficient K_1, but also with the disorientation angle (Fig. 6), i.e. the magnitude of the imposed displacement. Such a linear relationship, already pointed out by Britton et al. [38] regarding K_1 is actually well known in the literature. It is precisely used to estimate the first-order radial distortion by applying a planar translation to an object and measuring the error on the displacement and (phantom) strain field [57]. Regarding the magnitude of the error, it is of the order of 1 to 5×10^{-3} for a typical barrel distortion ($K_1 = -3\pm1\times10^{-8}$) in the presence of reasonably large rotations ($\Delta\theta \leq 8°$). This is consistent with the order of 10^{-3} announced by Britton et al. [38]. However, larger errors of the order of 10^{-2} can be made at larger rotations, especially for significant barrel distortion close to 10^{-7} as they did. A direct comparison of both studies is, however, hard since they cross-correlated distorted patterns with a distortion-free reference pattern, while all patterns undergo the same optical distortion in this work. Note that no distortion-free reference pattern was matched to optically distorted target patterns in this work for two reasons: (i) the use of a strain-free simulated reference is still limited by the uncertainty on the projection geometry [38,41,48,49], (ii) the errors would be greater than the presently observed ones [38], making the necessity of a correction even more crucial.

If both the reference and the test patterns are distorted in the same manner, Britton et al. [38] concluded that the optical distortions constitute a second-order issue, especially at low disorientation angles. They indeed noticed that neglecting a relatively large barrel distortion of 10^{-7} only induces an error of about 1.5% of the applied value on the worst-affected elastic strain component for a disorientation angle of 2.5°. The present study contradicts this statement. As highlighted in Fig. 5, neglecting a lower distortion of $K_1 = -3\times10^{-8}$ already induces

a maximum error (Eq. (21)) at least as high as the usually claimed accuracy of the HR-EBSD technique, i.e. 1×10^{-4}. Notable errors ranging from 5 to 8×10^{-4} are even observed although only a disorientation angle of barely 1° is considered. More than the level of the error itself, Fig. 7d-h showed that relative errors are quasi systematically higher than 10%. Relative errors of several tens to several hundred percent are even reached, especially when the elastic strain is below 2×10^{-3}, which is typical of the metallic materials investigated using HR-EBSD techniques.

Yet, all these observations are consistent with the previous study by Britton et al. [38]. The 1.5% error announced by the authors is actually obtained by dividing the 6.1×10^{-4} error on the worst-affected elastic strain component by the 4.4×10^{-2} (radians) applied rotation, instead of the applied strain which is zero in their study. The relative error on elastic strain is logically either indeterminate or infinite, but it is about 600% if a measurement noise of 1×10^{-4} is assumed. As pointed out by the grey region in Fig. 8a, the pure w_3 rotation they considered appears to be a specific case which tends to underestimate the error. Based on Fig. 8c, the present observations are quite generalisable since the position of the pattern centre with respect to the one of the optical centre only shows a marginal impact on the error induced by neglecting a radial distortion of $K_1 = -3\times10^{-8}$.

The proposed integrated correction offers a significant accuracy improvement (Fig. 4c-d) provided that the estimated correction parameters are reasonably close to the true ones. As highlighted in Fig. 9, an integer pixel accuracy on the optical centre coordinates as well as the uncertainty of 1×10^{-9} (3,3%) on the distortion coefficient K_1 of typical value -3×10^{-8} is sufficient to ensure the error does not exceed $\sim5\times10^{-5}$ for disorientation angles lower than 3° Such uncertainties correspond to the resolution of the values given by Mingard et al. [37]. Accounting for the optical distortions for accurate HR-EBSD measurement is thus not a hindrance as the determination of the projection geometry can be.

As shown in Section 2.5, the correction is not expected to extend the execution time of the IC-GN algorithm by more than 5–10%, depending on the complexity of the interpolation scheme and the distortion model. Since this percentage is evaluated from a fixed number of iterations, no direct conclusions should thus be drawn regarding the duration of the full analysis. On the one hand, the numerical cost of the integrated correction has to be compared to the one induced by the pattern pre-processing step conducted so far. On the other hand, it depends on the relative importance of the subpixel registration with respect to the other steps, namely the image filtering, the pre-computation of the interpolation coefficient, or the initial guess. The systematic use of the correction of the optical distortion is consequently recommended since a substantial or moderate gain in accuracy is then achievable at a small computation expense (depending on the elastic strain and disorientation levels, see Fig. 7). Of course, a suitable distortion model has to be used while the data and the SEM calibration should lend themselves to precise measurements.

In the present case, the integrated correction resulted in a shorter analysis than if the patterns had been pre-processed (i.e. interpolated once, in order to undistort them followed by the second interpolation to warp them during the subpixel registration). Indeed, computing the biquintic B-splines coefficients lasts as long as ~100 iterations of the IC-GN algorithm, which typically converged in 2 to 30 iterations. Note that the number of iterations is below 100 in Vermeij & Hoefnagels [30] when considering dynamically simulated patterns having between 10 and 20% noise, but also in Ernould et al. [16], where a 15% strained interstitial free steel specimen is investigated.

Ideally, the present work should be extended to more complex distortions models. A preliminary step would be to finely characterise the optical distortion of EBSD cameras. amongst the numerous methods for optical distortion measurement, the work by Dufour et al. [68] in which a printed calibration target is compared to its digital version has raised our attention in many ways. Not only this method has a particularly high resolution on displacements (up to $\sim2.5\times10^{-3}$ pixels), but it is also versatile and adaptable to different distortion models. Even more noticeable, it relies on a DIC approach based on parametric image registration similar to 'global' HR-EBSD approaches. Its integration in a 'global' HR-EBSD software would be, to our point of view, particularly relevant. Indeed, a part of the code could be common so that any improvement would be beneficial to both aspects, making the implementation task very effective.

Finally, the HR-EBSD technique should benefit from good practices and hardware improvements. amongst them, one example is turning on the camera about ~2 hours before the orientation map acquisition to prevent errors caused by the self-heating of the camera, in particular the one of the CCD [69]. This can also be limited by the use of high-quality bilateral telecentric lenses [70] (i.e. the entrance and exit pupils are at infinity). In addition, such lenses are subjected to significantly reduced optical distortions as compared to conventional ones. Aside from their cost, the limitations of such systems (fixed field of view with non-adjustable magnification and limited depth focus) do not concern EBSD cameras which film a fixed and flat scintillator.

6. Conclusions

Correction of the optical distortions caused by camera lenses has been integrated to the Gauss-Newton algorithm used by 'global' HR-EBSD approaches. The DIC analysis is thus applied to the experimental distorted patterns directly, avoiding their pre-processing without substantially impacting the numerical cost of the subpixel registration. The choice of the distortion model depends on the camera and can be set by the user. The correction's principle remains however unchanged. Here, it is implemented in the homography-based HR-EBSD approach and validated numerically for various levels of first-order radial distortion over a large range of disorientation angles (0 to 14°) and elastic strain levels (0 to 5×10^{-2}). Out of this, the following conclusions can be set up:

- Accounting for optical distortions is highly recommended for the accurate measurements of elastic strains in the typical range of 1×10^{-4} to 2×10^{-3}, even when disorientations below 1° and both distorted reference and target patterns are considered ($K_1 = -3\times10^{-8}$). Otherwise, a typical accuracy of $\sim1\times10^{-4}$ cannot be ensured. Moreover, relative errors from several tens to several hundred percent can be made on the elastic strain components.
- If a first-order radial distortion of coefficient K_1 is neglected, the induced error increases linearly with the absolute value of K_1 (barrel or pincushion distortions are equivalent). Another linear increase with the disorientation angle is observed whereas the elastic strains have marginal influence. The error remains relatively unaffected by the absolute position of the optical centre in the image or its position relative to the pattern centre.
- Neglecting a typical barrel distortion of -2 to -4×10^{-8} generates errors in the order of 1 to 5×10^{-3} on the elastic strain and lattice rotation components. An integer-pixel accuracy on the optical centre coordinates as well as a resolution of 1×10^{-9} on the first-order radial distortion coefficient ensures the correction effectiveness (i.e. the error here remains below 5×10^{-5}).
- The interpolation bias is a determining factor for the accuracy of the DIC analysis, in particular at low disorientation angles (<0.3–0.5°). Alone, it can limit the accuracy of the technique to 1×10^{-4} when the test patterns were generated using a bicubic interpolation.

Declaration of Competing Interest

The authors declare that they have no known competing financial interests or personal relationships that could have appeared to influence the work reported in this paper.

Appendices

A. *Left polar decomposition of the deformation gradient*

In ATEX-software [62], the singular value decomposition of the deformation gradient, $\mathbf{F}^e = \mathbf{W}.\boldsymbol{\Sigma}.\mathbf{V}^T$, where $\boldsymbol{\Sigma}$ is a 3×3 diagonal matrix containing the singular values while $\boldsymbol{W}$ and $\boldsymbol{V}$ are two 3×3 unitary matrices, is used to determine the left stretch tensor

$$\mathbf{v} = \mathbf{W}.\boldsymbol{\Sigma}.\mathbf{W}^T, \tag{A.1}$$

and the rotation matrix

$$\mathbf{R} = \mathbf{W}.\mathbf{V}^T. \tag{A.2}$$

By definition, the rotation matrix $\boldsymbol{R}$ is obtained from the three lattice rotations ω_i ($i \in [\![1,3]\!]$) as follows:

$$\boldsymbol{R} = \begin{pmatrix} c_2.c_3 & s_1.s_2.c_3 - c_1.s_3 & c_1.s_2.c_3 + s_1.s_3 \\ c_2.s_3 & s_1.s_2.s_3 + c_1.c_3 & c_1.s_2.s_3 - s_1.c_3 \\ -s_2 & s_1.c_2 & c_1.c_2 \end{pmatrix} \tag{A.3}$$

where $c_i = \cos(\omega_i)$ and $s_i = \sin(\omega_i)$. The lattice rotations are deduced as follows:

$$\omega_1 = \operatorname{atan}\left(\frac{R_{32}}{R_{33}}\right) + \eta.\pi \tag{A.4}$$

$$\omega_2 = \operatorname{atan}\left(-\frac{R_{31}}{\sqrt{R_{11}^2 + R_{21}^2}}\right) \tag{A.5}$$

$$\omega_3 = \operatorname{atan}\left(\frac{s_1.R_{13} - c_1.R_{12}}{c_1.R_{22} - s_1.R_{23}}\right) + \eta.\pi \tag{A.6}$$

where $\eta = \begin{cases} 1 & \text{if } \omega_2 = \pi/2 \\ 0 & \text{otherwise} \end{cases}$.

As shown in Eq. (3), the deduction of the elastic strain components from the left stretch tensor is simpler: $\boldsymbol{\varepsilon} = \boldsymbol{v} - \boldsymbol{I}$. However, this was found to be incorrect when considering the deviatoric deformation gradient $\widehat{\mathbf{F}^e}$ ($\widehat{F^e_{33}} = 1$), for which $\widehat{\boldsymbol{\varepsilon}} = \frac{1}{v_{33}}.(\boldsymbol{v} - v_{33}.\boldsymbol{I})$ should be used instead.

B. *Correction of the homography parameters*

The displacement by a vector $[\,\delta_1 \quad \delta_2\,]^T$ of the pattern centre of the target pattern with respect to the reference one generates a translation of the whole target pattern by this amount. This translation is modelled by the following matrix

$$\boldsymbol{T} = \begin{pmatrix} 1 & 0 & \delta_1 \\ 0 & 1 & \delta_2 \\ 0 & 0 & 1 \end{pmatrix} \tag{B.1}$$

since $x_i' = x_i + \delta_i$, which gives $\xi_i' = \xi_i + \delta_i$ after subtracting by x_{0i} ($i = 1,2$), i.e. by the relative coordinates of $\mathbf{X_0}$ with respect to the pattern centre ($\boldsymbol{\xi} = \mathbf{X} - \mathbf{X_0}$ and $\boldsymbol{\xi}' = \mathbf{X}' - \mathbf{X_0}$). Similarly, the displacement by $\delta DD.\overrightarrow{X_3}$ of the source point induces isotropic scaling of the pattern by a factor $\alpha = (DD - \delta DD)/DD$ with respect to the pattern centre. This scaling is expressed by the matrix

$$\boldsymbol{S} = \begin{pmatrix} \alpha & 0 & x_{01}.(\alpha - 1) \\ 0 & \alpha & x_{02}.(\alpha - 1) \\ 0 & 0 & 1 \end{pmatrix} \tag{B.2}$$

since $x_i' = \alpha.x_i$, which leads to $\xi_i' = \alpha.\xi_i + x_{0i}.(\alpha - 1)$ after noticing that $x_i' = \alpha.x_i + \alpha.x_{0i} - \alpha.x_{0i}$ and subtracting by x_{0i}.

The contribution of $\boldsymbol{T}$ and $\boldsymbol{S}$ has to be removed from the measured homography parameters h_{ij} before deducing the deformation gradient $\widehat{\mathbf{F}^e}$. When modelling the effects of a variation in the projection geometry, the order in which the scaling and the translation must be applied depends on the definition of the x_{0i} ($i = 1,\ 2$). Here, it is measured with respect to the pattern centre of the reference so the scaling has to be applied prior to the translation, i.e. the transformation is

$$\boldsymbol{T}.\boldsymbol{S} = \begin{pmatrix} \alpha & 0 & \delta_1 + x_{01}.(\alpha - 1) \\ 0 & \alpha & \delta_2 + x_{02}.(\alpha - 1) \\ 0 & 0 & 1 \end{pmatrix} \tag{B.3}$$

and not

$$\boldsymbol{S}.\boldsymbol{T} = \begin{pmatrix} \alpha & 0 & \alpha.\delta_1 + x_{01}.(\alpha-1) \\ 0 & \alpha & \alpha.\delta_2 + x_{02}.(\alpha-1) \\ 0 & 0 & 1 \end{pmatrix} \tag{B.4}$$

as indicated by the authors in [16] (the only difference is that the δ_i are no more multiplied by α).

The total transformation $\boldsymbol{W}$ measured by the DIC (Eq. (6)) can be actually viewed as $\boldsymbol{T}.\boldsymbol{S}.\widehat{\boldsymbol{W}}$, where $\widehat{\boldsymbol{W}}$ is the corrected homography associated with the transformation $\widehat{\mathbf{F}^e}$ in Eq. (9). The (undistorted) reference pattern is first warped according to $\widehat{\boldsymbol{W}}$. The so-obtained deformed pattern is then affected by variations of the projection geometry, which leads to the (undistorted) target pattern. The relationships giving the corrected deformation parameters $\widehat{h}_{ij}$ in Eq. (8) are consequently obtained by computing $\widehat{\boldsymbol{W}} = (\mathbf{T}.\mathbf{S})^{-1}.\mathbf{W}$ where

$$(\mathbf{T}.\mathbf{S})^{-1} = \begin{pmatrix} 1/\alpha & 0 & -\dfrac{\delta_1 + x_{01}.(\alpha-1)}{\alpha} \\ 0 & 1/\alpha & -\dfrac{\delta_2 + x_{02}.(\alpha-1)}{\alpha} \\ 0 & 0 & 1 \end{pmatrix}. \tag{B.5}$$

C. Simulation parameters in EMSoft 4.2

Table C.1 regroups the parameters used for the simulation of the diffraction pattern in EMsoft 4.2.

D. Inverse radial distortion coefficients

The following relationships are adapted from Drap et al. [53], where a radial distortion up to the fourth order (i.e. with 4 K_i coefficients) is exactly inverted using another radial distortion model, but of the ninth order. In the case of first-order radial distortion, the point of absolute coordinates $[X_1 \quad X_2]^T$ in the undistorted configuration admits for image $\left[\tilde{X}_1 \quad \tilde{X}_2\right]^T$ in the distorted configuration according to the distortion model

$$D : \begin{pmatrix} \tilde{X}_1 \\ \tilde{X}_2 \end{pmatrix} = \begin{pmatrix} X_1 \\ X_2 \end{pmatrix} + K_1.r^2.\begin{pmatrix} \Delta_1 \\ \Delta_2 \end{pmatrix} \tag{D.1}$$

where $r = \sqrt{\Delta_1^2 + \Delta_2^2}$ with $\Delta_i = X_i - X_i^{opt}$ $(i = 1,2)$, the X_i^{opt} being the absolute coordinates of the optical centre. The inverse distortion model

$$D^{-1} : \begin{pmatrix} X_1 \\ X_2 \end{pmatrix} = \begin{pmatrix} \tilde{X}_1 \\ \tilde{X}_2 \end{pmatrix} + \sum_{i=1}^{9} b_i.r^{2i}.\begin{pmatrix} \Delta_1 \\ \Delta_2 \end{pmatrix} \tag{D.2}$$

where $\Delta_i = \tilde{X}_i - X_i^{opt}$ $(i = 1,2)$ involves nine coefficients b_i which are analytically deduced from K_1 according to Eq. (D.3) to (D.11).

$$b_1 = -K_1 \tag{D.3}$$

$$b_2 = 3.K_1^2 \tag{D.4}$$

Table C.1
Parameters of the dynamical pattern simulation in EMsoft 4.2.

Material		**Pattern simulation parameters**	
Element	Aluminium	Camera tilt angle	0°
Structure	FCC	Euler angles	(75°, 125°, 15°)
Lattice parameter	0.4 nm	Detector size	2400 × 2400
Debye-Waller factor	0.004 nm^2	Pixel size	20 μm
		DD	16 mm
Monte Carlo simulation parameters		PCx, PCy	0, 0
Number of electrons	2×10^9	Bit depth	16-bit (integer)
Specimen tilt angle	70°	Incident beam current	150 nA
Incident beam energy	20 keV	Beam dwell time	100 μs
Minimum energy to consider	15 keV	Energy range (min)	20 keV
Energy bin size	1 keV	Energy range (max)	20 keV
Maximum exit depth	100 nm	Include background	no
Depth step size	1 nm	Include noise	no
		Gamma value	0.33
Master pattern simulation parameters			
Smallest d-spacing	0.05 nm		
Master pattern size	1000 (2001 × 2001)		
Bethe parameters	4 / 8 / 50		

$$b_3 = -12.K_1^3 \tag{D.5}$$

$$b_4 = 55.K_1^4 \tag{D.6}$$

$$b_5 = -273.K_1^5 \tag{D.7}$$

$$b_6 = 1428.K_1^6 \tag{D.8}$$

$$b_7 = -7752.K_1^7 \tag{D.9}$$

$$b_8 = 43,263.K_1^8 \tag{D.10}$$

$$b_9 = -246,675.K_1^9 \tag{D.11}$$

E. *Initialisation of the homography*

The height deformation parameters h_{ij} of the homography are initialised from the cross-correlation based initial guess introduced in [16]. Its implementation has been improved and the target subset is now rotated, instead of the reference one. As illustrated in Fig. E.1. It first estimates the in-plane rotation θ_0 around $\overrightarrow{X_3}$ between the target subset and the reference subset. The target subset is then rotated by $-\theta_0$ with respect to its centre. Finally, the remaining translation $t_1.\overrightarrow{X_1} + t_2.\overrightarrow{X_2}$ between the so-obtained subset and the reference subset is measured.

As indicated by Fig. E.1, the rigid transformation from the reference configuration to the deformed configuration is obtained by applying the measured translation, and then the rotation of angle θ_0 with respect to $\mathbf{X_0}$. It is described by the following deformation parameters:

$$\begin{bmatrix} h_{11}+1 & h_{12} & h_{13} \\ h_{21} & h_{22}+1 & h_{23} \\ h_{31} & h_{32} & 1 \end{bmatrix} = \begin{bmatrix} \cos(\theta_0) & -\sin(\theta_0) & t_1.\cos(\theta_0) - t_2.\sin(\theta_0) \\ \sin(\theta_0) & \cos(\theta_0) & t_1.\sin(\theta_0) + t_2.\cos(\theta_0) \\ 0 & 0 & 1 \end{bmatrix}, \tag{E.1}$$

which is designated in [16] as the 'partial' initialisation of the homography since h_{31} and h_{32} are left equal to zero. The 'complete' initialisation of the homography is achieved by first estimating the three lattice rotations ω_i in the detector frame, from which the rotation matrix $\boldsymbol{R}$ is deduced (see Eq. (A.3)). The h_{ij} parameters are then analytically deduced from $\widehat{\boldsymbol{R}} = \boldsymbol{R}/R_{33}$ conversely to Eq. (9) (see [16] for more details).

As a consequence of the improvements brought to the code as compared to [16], the lattice rotations are estimated from the cross-correlation based measurements as follows:

$$\omega_1 = atan\left(\frac{-\Delta_2}{DD}\right) \text{ with } \Delta_2 = t_2 - x_{01}.\sin(\theta_0) + x_{02}.(cos(\theta_0) - 1) \tag{E.2}$$

$$\omega_2 = atan\left(\frac{\Delta_1}{DD}\right) \text{ with } \Delta_1 = t_1 + x_{01}.(cos(\theta_0) - 1) + x_{02}.\sin(\theta_0) \tag{E.3}$$

$$\omega_3 = \theta_0 \tag{E.4}$$

Equations (E.2) and (E.3) are obtained by stating that the image of a point by the rigid transformation in equation (E.1),

$$\begin{cases} \xi_1' = \cos(\theta_0).\xi_1 - \sin(\theta_0).\xi_2 + \cos(\theta_0).t_1 - \sin(\theta_0).t_2 \\ \xi_2' = \sin(\theta_0).\xi_1 + \cos(\theta_0).\xi_2 + \sin(\theta_0).t_1 + \cos(\theta_0).t_2 \end{cases}, \tag{E.5}$$

has to match the image of a point by a translation $\Delta_1.\overrightarrow{X_1} + \Delta_2.\overrightarrow{X_2}$ followed by a rotation of angle θ_0 with respect to the pattern centre (not X_0):

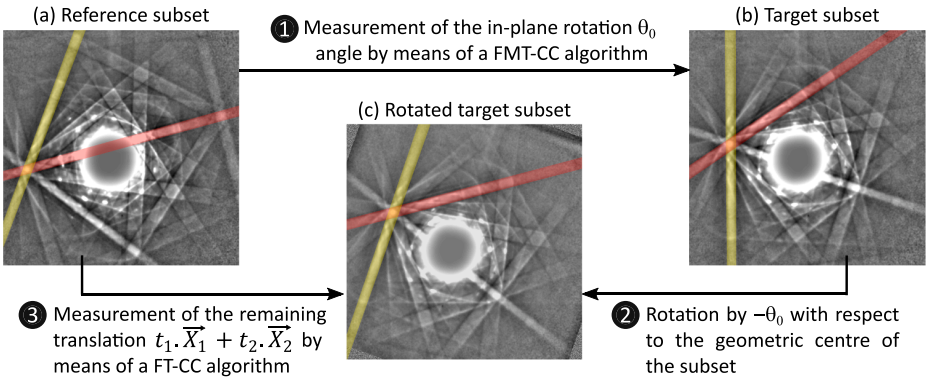

Fig. E.1. Illustration of the working principle of the global cross-correlation based initial guess. Note that the on-axis TKD patterns are the same as the one used in [16].

$$\begin{cases} \xi_1' = \cos(\theta_0).x_1 - \sin(\theta_0).x_2 + \cos(\theta_0).\Delta_1 - \sin(\theta_0).\Delta_2 - x_{01} \\ \xi_2' = \sin(\theta_0).x_1 + \cos(\theta_0).x_2 + \sin(\theta_0).\Delta_1 + \cos(\theta_0).\Delta_2 - x_{02} \end{cases}. \tag{E.6}$$

Note that by definition of $\boldsymbol{\xi}$ and $\boldsymbol{\xi}'$: $\xi_i' = x_i' - x_{0i}$ and $x_i - \xi_i = x_{0i}$. Moreover, the projection geometry (i.e. x_{01}, x_{02}, and DD) does not need to be very accurate at this stage since it is the initial guess.

References

[1] J.A. Venables, C.J. Harland, Electron back-scattering patterns—a new technique for obtaining crystallographic information in the scanning electron microscope, Philos. Mag. 27 (1973) 1193–1200.

[2] R.R. Keller, R.H. Geiss, Transmission EBSD from 10 nm domains in a scanning electron microscope, J. Microsc. 245 (2012) 245–251, https://doi.org/10.1111/j.1365-2818.2011.03566.x.

[3] J.J. Fundenberger, E. Bouzy, D. Goran, J. Guyon, H. Yuan, A. Morawiec, Orientation mapping by transmission-SEM with an on-axis detector, Ultramicroscopy 161 (2016) 17–22, https://doi.org/10.1016/j.ultramic.2015.11.002.

[4] N.C. Krieger Lassen, K. Conradsen, D. Juul Jensen, Image processing procedures for analysis of electron diffraction patterns, Scann. Microsc. 6 (1992) 115–121.

[5] S.I. Wright, J.A. Basinger, M.M. Nowell, Angular precision of automated electron backscatter diffraction measurements, Mater. Sci. Forum. 702–703 (2012) 548–553, 10.4028/, www.scientific.net/MSF.702-703.548.

[6] Y.-H. Chen, S.U. Park, D. Wei, G. Newstadt, M. Jackson, J.P. Simmons, M. De Graef, A.O. Hero, A dictionary approach to EBSD indexing, ArXiv150207436, Phys. Stat. (2015). http://arxiv.org/abs/1502.07436 (accessed March 5, 2019).

[7] R. Hielscher, F. Bartel, T.B. Britton, Gazing at crystal balls - Electron backscatter diffraction indexing and cross correlation on a sphere, ArXiv181003211, Cond-Mat. (2018). http://arxiv.org/abs/1810.03211 (accessed May 6, 2019).

[8] W.C. Lenthe, S. Singh, M.D. Graef, A spherical harmonic transform approach to the indexing of electron back-scattered diffraction patterns, Ultramicroscopy 207 (2019), 112841, https://doi.org/10.1016/j.ultramic.2019.112841.

[9] G. Nolze, A. Winkelmann, A.P. Boyle, Pattern matching approach to pseudosymmetry problems in electron backscatter diffraction, Ultramicroscopy 160 (2016) 146–154, https://doi.org/10.1016/j.ultramic.2015.10.010.

[10] T. Friedrich, A. Bochmann, J. Dinger, S. Teichert, Application of the pattern matching approach for EBSD calibration and orientation mapping, utilising dynamical EBSP simulations, Ultramicroscopy 184 (2018) 44–51, https://doi.org/10.1016/j.ultramic.2017.10.006.

[11] A. Winkelmann, B.M. Jablon, V.S. Tong, C. Trager-Cowan, K.P. Mingard, Improving EBSD precision by orientation refinement with full pattern matching, J. Microsc. 277 (2020) 79–92, https://doi.org/10.1111/jmi.12870.

[12] F. Ram, S. Wright, S. Singh, M.D. Graef, Error analysis of the crystal orientations obtained by the dictionary approach to EBSD indexing, Ultramicroscopy 181 (2017) 17–26, https://doi.org/10.1016/j.ultramic.2017.04.016.

[13] S. Singh, Y. Guo, B. Winiarski, T.L. Burnett, P.J. Withers, M.D. Graef, High resolution low kV EBSD of heavily deformed and nanocrystalline Aluminium by dictionary-based indexing, Sci. Rep. 8 (2018) 1–8, https://doi.org/10.1038/s41598-018-29315-8.

[14] D.J. Prior, Problems in determining the misorientation axes, for small angular misorientations, using electron backscatter diffraction in the SEM. J. Microsc. 195 (1999) 217–225.

[15] M.C. Demirel, B.S. El-Dasher, B.L. Adams, A.D. Rollett, Studies on the accuracy of electron backscatter diffraction measurements, in: A.J. Schwartz, M. Kumar, B. L. Adams (Eds.), Electron Backscatter Diffr. Mater. Sci., Springer US, Boston, MA, 2000, pp. 65–74, https://doi.org/10.1007/978-1-4757-3205-4_6.

[16] C. Ernould, B. Beausir, J.-J. Fundenberger, V. Taupin, E. Bouzy, Global DIC approach guided by a cross-correlation based initial guess for HR-EBSD and on-axis HR-TKD, Acta Mater. 191 (2020) 131–148, https://doi.org/10.1016/j.actamat.2020.03.026.

[17] K.Z. Troost, P. van der Sluis, D.J. Gravesteijn, Microscale elastic-strain determination by backscatter Kikuchi diffraction in the scanning electron microscope, Appl. Phys. Lett. 62 (1993) 1110–1112, https://doi.org/10.1063/1.108758.

[18] A.J. Wilkinson, Advances in SEM–based diffraction studies of defects and strains in semiconductors, J. Electron. Microsc. (Tokyo). 49 (2000) 299–310, https://doi.org/10.1093/oxfordjournals.jmicro.a023810.

[19] A. Wilkinson, A new method for determining small misorientations from EBSD patterns, Scr. Mater. 44 (2001) 2379–2385.

[20] A.J. Wilkinson, G. Meaden, D.J. Dingley, High-resolution elastic strain measurement from electron backscatter diffraction patterns: new levels of sensitivity, Ultramicroscopy 106 (2006) 307–313, https://doi.org/10.1016/j.ultramic.2005.10.001.

[21] S. Villert, C. Maurice, C. Wyon, R. Fortunier, Accuracy assessment of elastic strain measurement by EBSD, J. Microsc. 233 (2009) 290–301, https://doi.org/10.1111/j.1365-2818.2009.03120.x.

[22] T.B. Britton, A.J. Wilkinson, Measurement of residual elastic strain and lattice rotations with high resolution electron backscatter diffraction, Ultramicroscopy 111 (2011) 1395–1404, https://doi.org/10.1016/j.ultramic.2011.05.007.

[23] A.J. Wilkinson, G. Meaden, D.J. Dingley, High resolution mapping of strains and rotations using electron backscatter diffraction, Mater. Sci. Technol. 22 (2006) 1271–1278, https://doi.org/10.1179/174328406X130966.

[24] T.B. Britton, A.J. Wilkinson, High resolution electron backscatter diffraction measurements of elastic strain variations in the presence of larger lattice rotations, Ultramicroscopy 114 (2012) 82–95, https://doi.org/10.1016/j.ultramic.2012.01.004.

[25] T.J. Hardin, T.J. Ruggles, D.P. Koch, S.R. Niezgoda, D.T. Fullwood, E.R. Homer, Analysis of traction-free assumption in high-resolution EBSD measurements, J. Microsc. 260 (2015) 73–85, https://doi.org/10.1111/jmi.12268.

[26] B. Pan, Y. Wang, L. Tian, Automated initial guess in digital image correlation aided by Fourier–Mellin transform, Opt. Eng. 56 (2017), 0141031, https://doi.org/10.1117/1.OE.56.1.014103.

[27] C. Maurice, J.H. Driver, R. Fortunier, On solving the orientation gradient dependency of high angular resolution EBSD, Ultramicroscopy 113 (2012) 171–181, https://doi.org/10.1016/j.ultramic.2011.10.013.

[28] C. Zhu, K. Kaufmann, K.S. Vecchio, Novel remapping approach for HR-EBSD based on demons registration, Ultramicroscopy 208 (2020), 112851, https://doi.org/10.1016/j.ultramic.2019.112851.

[29] B. Pan, Digital image correlation for surface deformation measurement: historical developments, recent advances and future goals, Meas. Sci. Technol. 29 (2018), 082001, https://doi.org/10.1088/1361-6501/aac55b.

[30] T. Vermeij, J.P.M. Hoefnagels, A consistent full-field integrated DIC framework for HR-EBSD, Ultramicroscopy 191 (2018) 44–50, https://doi.org/10.1016/j.ultramic.2018.05.001.

[31] T.J. Ruggles, G.F. Bomarito, R.L. Qiu, J.D. Hochhalter, New levels of high angular resolution EBSD performance via inverse compositional Gauss–Newton based digital image correlation, Ultramicroscopy 195 (2018) 85–92, https://doi.org/10.1016/j.ultramic.2018.08.020.

[32] Q. Shi, S. Roux, F. Latourte, F. Hild, Estimation of elastic strain by integrated image correlation on electron diffraction patterns, Ultramicroscopy 199 (2019) 16–33, https://doi.org/10.1016/j.ultramic.2019.02.001.

[33] V. Tong, J. Jiang, A.J. Wilkinson, T.B. Britton, The effect of pattern overlap on the accuracy of high resolution electron backscatter diffraction measurements, Ultramicroscopy 155 (2015) 62–73, https://doi.org/10.1016/j.ultramic.2015.04.019.

[34] J. Jiang, T.B. Britton, A.J. Wilkinson, Measurement of geometrically necessary dislocation density with high resolution electron backscatter diffraction: effects of detector binning and step size, Ultramicroscopy 125 (2013) 1–9, https://doi.org/10.1016/j.ultramic.2012.11.003.

[35] T.B. Britton, J. Jiang, R. Clough, E. Tarleton, A.I. Kirkland, A.J. Wilkinson, Assessing the precision of strain measurements using electron backscatter diffraction – part 1: detector assessment, Ultramicroscopy 135 (2013) 126–135, https://doi.org/10.1016/j.ultramic.2013.08.005.

[36] A.P. Day, Spherical EBSD, J. Microsc. 230 (2008) 472–486, https://doi.org/10.1111/j.1365-2818.2008.02011.x.

[37] K. Mingard, A. Day, C. Maurice, P. Quested, Towards high accuracy calibration of electron backscatter diffraction systems, Ultramicroscopy 111 (2011) 320–329, https://doi.org/10.1016/j.ultramic.2011.01.012.

[38] T.B. Britton, C. Maurice, R. Fortunier, J.H. Driver, A.P. Day, G. Meaden, D. J. Dingley, K. Mingard, A.J. Wilkinson, Factors affecting the accuracy of high resolution electron backscatter diffraction when using simulated patterns, Ultramicroscopy 110 (2010) 1443–1453, https://doi.org/10.1016/j.ultramic.2010.08.001.

[39] V. Randle, O. Engler, Introduction to Texture analysis: macrotexture, Microtexture and Orientation Mapping, Gordon and Breach, Amsterdam, 2000.

[40] T. Tanaka, A.J. Wilkinson, Pattern matching analysis of electron backscatter diffraction patterns for pattern centre, crystal orientation and absolute elastic strain determination – accuracy and precision assessment, Ultramicroscopy 202 (2019) 87–99, https://doi.org/10.1016/j.ultramic.2019.04.006.

[41] C. Maurice, R. Fortunier, J. Driver, A. Day, K. Mingard, G. Meaden, Comments on the paper “Bragg’s law diffraction simulations for electron backscatter diffraction analysis” by Josh Kacher, Colin Landon, Brent L. Adams & David Fullwood, Ultramicroscopy 110 (2010) 758–759, https://doi.org/10.1016/j.ultramic.2010.02.003.

[42] C. Maurice, K. Dzieciol, R. Fortunier, A method for accurate localisation of EBSD pattern centres, Ultramicroscopy 111 (2011) 140–148, https://doi.org/10.1016/j.ultramic.2010.10.007.

[43] J. Basinger, D. Fullwood, J. Kacher, B. Adams, Pattern center determination in electron backscatter diffraction microscopy, Microsc. Microanal. 17 (2011) 330–340, https://doi.org/10.1017/S1431927611000389.

[44] J. Alkorta, M. Marteleur, P.J. Jacques, Improved simulation based HR-EBSD procedure using image gradient based DIC techniques, Ultramicroscopy 182 (2017) 17–27, https://doi.org/10.1016/j.ultramic.2017.06.015.

[45] E.L. Pang, P.M. Larsen, C.A. Schuh, Global optimization for accurate determination of EBSD pattern centers, Ultramicroscopy 209 (2020), 112876, https://doi.org/10.1016/j.ultramic.2019.112876.
[46] A. Winkelmann, G. Nolze, G. Cios, T. Tokarski, P. Bała, Refined calibration model for improving the orientation precision of electron backscatter diffraction maps, Mater. (Basel) 13 (2020) 2816, https://doi.org/10.3390/ma13122816.
[47] J. Kacher, C. Landon, B.L. Adams, D. Fullwood, Bragg's Law diffraction simulations for electron backscatter diffraction analysis, Ultramicroscopy 109 (2009) 1148–1156, https://doi.org/10.1016/j.ultramic.2009.04.007.
[48] J. Alkorta, Limits of simulation based high resolution EBSD, Ultramicroscopy 131 (2013) 33–38, https://doi.org/10.1016/j.ultramic.2013.03.020.
[49] T. Vermeij, M. De Graef, J. Hoefnagels, Demonstrating the potential of accurate absolute cross-grain stress and orientation correlation using electron backscatter diffraction, Scr. Mater. 162 (2019) 266–271, https://doi.org/10.1016/j.scriptamat.2018.11.030.
[50] D.C. Brown, Close-range camera calibration, Photogramm. Eng. 37 (1971) 855–866.
[51] D.H. Brown, Decentering distortion of lenses, Photom. Eng. 32 (1966) 444–462.
[52] A.E. Conrady, Decentering lens systems, Mon. Not. R. Astron. Soc. 79 (1919) 384–390, https://doi.org/10.1093/mnras/79.5.384.
[53] P. Drap, J. Lefèvre, An exact formula for calculating inverse radial lens distortions, Sensors (2016) 16, https://doi.org/10.3390/s16060807.
[54] R. Tsai, A versatile camera calibration technique for high-accuracy 3D machine vision metrology using off-the-shelf TV cameras and lenses, IEEE J. Robot. Autom. 3 (1987) 323–344, https://doi.org/10.1109/JRA.1987.1087109.
[55] S. Yoneyama, H. Kikuta, A. Kitagawa, K. Kitamura, Lens distortion correction for digital image correlation by measuring rigid body displacement, Opt. Eng. 45 (2006), 023602, https://doi.org/10.1117/1.2168411.
[56] J. Wang, F. Shi, J. Zhang, Y. Liu, A new calibration model of camera lens distortion, Pattern Recognit. 41 (2008) 607–615, https://doi.org/10.1016/j.patcog.2007.06.012.
[57] B. Pan, L. Yu, D. Wu, L. Tang, Systematic errors in two-dimensional digital image correlation due to lens distortion, Opt. Lasers Eng. 51 (2013) 140–147, https://doi.org/10.1016/j.optlaseng.2012.08.012.
[58] Z. Tang, R. Grompone von Gioi, P. Monasse, J.-.M. Morel, A precision analysis of camera distortion models, IEEE Trans. Image Process. 26 (2017) 2694–2704, https://doi.org/10.1109/TIP.2017.2686001.
[59] S. Baker, I. Matthews, Lucas-Kanade 20 years on: a unifying framework, Int. J. Comput. Vis. 56 (2004) 221–255, https://doi.org/10.1023/B:VISI.0000011205.11775.fd.
[60] B. Pan, K. Li, W. Tong, Fast, robust and accurate digital image correlation calculation without redundant computations, Exp. Mech. 53 (2013) 1277–1289, https://doi.org/10.1007/s11340-013-9717-6.
[61] J. Blaber, B. Adair, A. Antoniou, Ncorr: open-source 2D digital image correlation matlab software, Exp. Mech. 55 (2015) 1105–1122, https://doi.org/10.1007/s11340-015-0009-1.
[62] B. Beausir, J.-.J. Fundengerger, Analysis Tools for Electron and X-ray Diffraction, ATEX - Software, Université de Lorraine, Metz, 2017. www.atex-software.eu.
[63] S. Singh, F. Ram, M.D. Graef, EMsoft: open source software for electron diffraction/image simulations, Microsc. Microanal. 23 (2017) 212–213, https://doi.org/10.1017/S143192761700174X.
[64] H. Yu, J. Liu, P. Karamched, A.J. Wilkinson, F. Hofmann, Mapping the full lattice strain tensor of a single dislocation by high angular resolution transmission Kikuchi diffraction (HR-TKD), Scr. Mater. 164 (2019) 36–41, https://doi.org/10.1016/j.scriptamat.2018.12.039.
[65] M.J. McLean, W.A. Osborn, In-situ elastic strain mapping during micromechanical testing using EBSD, Ultramicroscopy 185 (2018) 21–26, https://doi.org/10.1016/j.ultramic.2017.11.007.
[66] M. Bornert, P. Doumalin, J.-.C. Dupré, C. Poilane, L. Robert, E. Toussaint, B. Wattrisse, Shortcut in DIC error assessment induced by image interpolation used for subpixel shifting, Opt. Lasers Eng. 91 (2017) 124–133, https://doi.org/10.1016/j.optlaseng.2016.11.014.
[67] C. Ernould, B. Beausir, J.-.J. Fundenberger, V. Taupin, E. Bouzy, Characterization at high spatial and angular resolutions of deformed nanostructures by on-axis HR-TKD, Scr. Mater. 185 (2020) 30–35, https://doi.org/10.1016/j.scriptamat.2020.04.005.
[68] J.-.E. Dufour, F. Hild, S. Roux, Integrated digital image correlation for the evaluation and correction of optical distortions, Opt. Lasers Eng. 56 (2014) 121–133, https://doi.org/10.1016/j.optlaseng.2013.12.015.
[69] S. Ma, J. Pang, Q. Ma, The systematic error in digital image correlation induced by self-heating of a digital camera, Meas. Sci. Technol. 23 (2012), 025403, https://doi.org/10.1088/0957-0233/23/2/025403.
[70] B. Pan, L. Yu, D. Wu, High-accuracy 2D digital image correlation measurements with bilateral telecentric lenses: error analysis and experimental verification, Exp. Mech. 53 (2013) 1719–1733, https://doi.org/10.1007/s11340-013-9774-x.